Journal of Inflammation Research

Dovepress
Taylor & Francis Group

Open Access Full Text Article

ORIGINAL RESEARCH

Identifying Immuno-Fibrotic Roles of Lactylation-Related T Cell Hub Genes in Renal Ischemia–Reperfusion Injury: A Multi-Omics Study and Experimental Validation

Xuemeng Qiu[1,2,*], Hao Wang[1,2,*], Yifei Zhang[1,2,*], Zhen Li[1,2], Jiyue Wu[1,2], Zejia Sun[1,2], Wei Wang[1,2]

[1]Department of Urology, Beijing Chao-Yang Hospital, Capital Medical University, Beijing, People's Republic of China; [2]Institute of Urology, Capital Medical University, Beijing, People's Republic of China

*These authors contributed equally to this work

Correspondence: Zejia Sun; Wei Wang, Department of Urology, Beijing Chao-Yang Hospital, Capital Medical University, 8 Gongrentiyuchang South Road, Chaoyang District, Beijing, 100020, People's Republic of China, Email mnwkszj5076@163.com; weiwang0920@163.com

Purpose: Renal ischemia-reperfusion injury (IRI) is a major posttransplant complication that promotes maladaptive repair and fibrosis, leading to allograft failure. However, the role of lactylation in these processes remains unclear. This study aimed to identify lactylation-associated biomarkers and their therapeutic potential in the IRI-induced maladaptive repair of kidney allografts and subsequent fibrosis.

Methods: A gene set encompassing genes involved in the enzymatic regulation of lactylation was summarized, which includes key substrate proteins, lactylation "writers" and "erasers". Single-cell RNA-seq data were used to identify overall and cell-specific lactylation activity after IRI and in fibrotic samples. hdWGCNA analysis was used to identify hub genes, followed by predictive model construction using machine-learning algorithms. The relationships between hub genes and renal function, immune cell infiltration, and fibrotic biomarkers were also analyzed. Pseudotime trajectory analysis was used to investigate hub genes expression changes along fibrosis progression. Finally, RT-qPCR of hub genes and immunohistochemical staining were performed in a mouse model of unilateral IRI-fibrosis fibrosis.

Results: Lactylation activity was elevated after IRI and in fibrotic samples, particularly in a subset of T cells, highlighting its importance in fibrogenesis. Four hub genes (HLA-E, IGHM, CORO1A, and TUBA1A) emerged as fibrosis biomarkers and showed robust predictive value for patient and graft survival (area under the curve of 0.83, 0.86, and 0.87 at 1, 2, and 3 years, respectively). Drug sensitivity and molecular docking analyses revealed the potential for repurposing existing drugs to target these genes. Lastly, experimental validation confirmed the increased mRNA expression of the hub genes.

Conclusion: This multi-omics study identified a key lactylation-associated hub T cell potentially implicated in post-IRI induced maladaptive repair. Four lactylation-related T-cell biomarkers (CORO1A, HLA-E, IGHM, and TUBA1A) predicted allograft maladaptive repair and survival, providing a precise framework for early risk stratification and potential therapeutic intervention.

Keywords: lactylation, lactate, T cell, kidney transplantation, molecular docking, fibrosis, ischemia-reperfusion injury

Introduction

Ischemia reperfusion injury (IRI) is an evitable event in kidney transplantation and a major contributor to delayed graft function and long-term graft loss. IRI substantially increases the risk of chronic allograft dysfunction (CAD), characterized by interstitial fibrosis and tubular atrophy.[1] CAD remains a leading cause of graft loss within the first decade post-transplantation.[2] Current strategies remain largely ineffective in preventing or reversing fibrotic progression, underscoring the need to identify pathological mechanisms and therapeutic targets.[3]

Received: 21 June 2025
Accepted: 25 September 2025
Published: 6 October 2025

Mechanistic studies have demonstrated that multiple processes drive the transition from acute kidney injury (AKI) to chronic kidney disease (CKD), including renal parenchyma injury,[4] vascular rarefaction,[5] and immune filtration.[6] Notably, leukocyte infiltration has emerged as an important determinant of graft outcomes. IRI enhances immunogenicity through parenchymal necrotic cell death and necroinflammation, as well as by accelerating antigen processing, collectively promote effector T cell recognition and infiltration.[7] Indeed, targeting immune cells has been proven effective in alleviating IRI-induced AKI.[8]

Recent work has highlighted the role of metabolic reprogramming in shaping immune and fibrotic responses.[9,10] Histone lactylation, a novel epigenetic modification driven by lactate accumulation, regulates gene expression and cell functions.[11] This modification has gained increasing attention in IRI and fibrosis research, owing to the interconnected roles of hypoxia, glycolysis, and lactate. During ischemia, cells rapidly shift toward glycolysis to maintain ATP production; however, sustained glycolysis and persistent lactate accumulation promote inflammation.[12] Mechanistically, metabolic reprogramming toward glycolysis promotes various cellular transitions: epithelial-to-mesenchymal transition,[13] endothelial-to-mesenchymal transition,[14] macrophage-to-myofibroblast transition,[15] and myofibroblast differentiation.[16] The glycolysis rate-limiting enzyme 6-phosphofructo-2-kinase/ fructose-2,6-biphosphatase 3 (PFKFB3) exacerbates IRI-induced kidney fibrosis by mediating tubular glycolytic reprogramming and inducing histone lactylation of NF-κB signaling genes, thereby promoting an inflammatory response. Targeted deletion of PFKFB3 in proximal tubular cells reduces lactate levels and mitigates inflammation and kidney fibrosis.[17] Additionally, the cyclic GMP-AMP synthase (cGAS) - stimulator of interferon genes (STING) signaling pathway enhances kidney IRI fibrosis by upregulating PFKFB3, highlighting the importance of glycolysis-related lactylation in the IRI-fibrosis process.[18]

Beyond parenchumal responses, lactylation also regulates immune cell functions during IRI and fibrosis. Inhibition of high mobility group box 1 (HMGB1) lactylation attenuates liver IRI and reduces macrophage infiltration,[19] while lactate-driven HMGB1 lactylation promoted neutrophil extracellular trap (NET) formation and worsens AKI.[20] Macrophages exposed to IRI underwent significant alterations in histone lactylation and related transcriptional profiles.[9] In pulmonary fibrosis, lactate produced by myofibroblasts drives histone lactylation via p300 in alveolar macrophages, skewing them toward a pro-fibrotic phenotype.[21] Despite these emerging findings, the contribution of lactylation to kidney allograft fibrosis, particularly within immune populations such as T cells, remains largely unexplored.

This study explored the role of lactylation in allograft fibrosis following IRI, and its contribution to maladaptive repair progression. Using single-cell RNA sequencing (scRNA-seq), we identified a T-cell subpopulation with significantly upregulated lactylation activity after IRI. Using single-cell high-dimensional weighted gene co-expression network analysis (hdWGCNA), we identified cell-specific lactylation-related genes (LRGs) in T-cells. Using various machine learning algorithms, we selected key LRGs to assess their diagnostic potential for allograft fibrosis, and built a prognostic model for predicting allograft failure. We investigated the downstream pathways of hub LRGs and upstream regulatory factors, conducted drug sensitivity and molecular docking analyses to identify potential therapeutic targets, and validated our findings using an in vivo unilateral IRI mouse model.

Materials and Methods

Data Acquisition and Preprocessing

The scRNA-seq dataset GSE180420 was downloaded from the Gene Expression Omnibus (GEO) database (https://www.ncbi.nlm.nih.gov/geo/). We analyzed 18 mouse kidney samples subjected to IRI, consisting of 6 control samples, 6 samples with short ischemia, and 6 samples with long ischemia, collected at 1, 3, and 14 days post-surgery.[22] The "Seurat" package (version 5.1.0) was used to analyze scRNA-seq data. Based on the prerequisites provided by the authors, we used the uniform manifold approximation and projection (UMAP) to visualize and cluster cell types across samples.[22] For sub-clustering of the T cell_2 cluster, initial quality control was performed by filtering out poor-quality cells with fewer than 200 or more than 3,000 expressed genes, and a mitochondrial ratio exceeding 0.2. Following normalization and principal component analysis (PCA), we performed dimensionality reduction using UMAP and clustered the cells at a resolution of 0.5. Subsequent analysis revealed contamination by cells expressing myeloid lineage markers, which were identified and removed. The above processing workflow was subsequently repeated with an

adjusted resolution of 0.4 to achieve optimal clustering. We also applied "FindAllMarkers" to identify cluster markers, with parameters test.use = "MAST", min.pct = 0.5, with a logfc.threshold = 0.2. Cell clusters were manually annotated using canonical markers of T lymphocytes and the top 10 genes with the highest log fold change (log FC), referencing marker genes from CellMarker 2.0 database.[23]

To investigate the long-term effects of key genes and their roles in allograft fibrosis, we obtained additional microarray datasets from the GEO database containing pathologically verified normal and interstitial fibrosis and tubular atrophy (IFTA) human kidney allograft biopsies (GSE53605,[24] GSE76882,[25] GSE22459,[26] and GSE21374.[27] The GSE21374 dataset also includes patient and graft survival information. Subsequently, the "affy" R package was used for normalization and standardization of the four datasets, where normalization was performed using the "rma" function, which applies quantile normalization. We combined GSE53605, GSE76882, and GSE22459 into a large dataset, while dataset-specific batch effects were then adjusted using the "removeBatchEffect" function from the "limma" package with default parameters. All the datasets used are summarized in Table 1.

In total, we downloaded LRGs from various sources, including Molecular Signatures Database (https://www.gsea-msigdb.org/gsea/msigdb) and previously published high-impact papers.[11,28,29] After removing duplicates, we obtained a total of 332 LRGs (Table S1). The LRGs used included histone acetyltransferase EP300, histone lysine delactylases class I histone deacetylases (HDAC1-3), nicotine adenine dinucleotide (+)-dependent histone deacetylases SIRT 1–3 etc. The study design is illustrated in Figure 1.

Mice, Unilateral IRI Model, Serum Creatinine Measurement and Tissue Collection

All surgical procedures, mouse handling, and husbandry were performed according to the guidelines of the Institutional Animal Care Ethics Committee of Beijing Chaoyang Hospital (Ethics No. 24–2016).

C57BL/6 mice (8-week-old) were provided by Beijing SiPeiFu Laboratory (Beijing, China). Mice were anesthetized with pentobarbital via intraperitoneal injection. After shaving the abdominal hair, an abdominal midline incision was made and the left renal pedicle was identified and clipped using an atraumatic clamp for 45 min. During the ischemic period, the body temperature of mice was maintained at 37 °C using a thermostatically controlled heating table The clamp was then removed and the peritoneum was closed with 5–0 suture. The other renal pedicle and kidney is intact. In the sham group, the abdomen was exposed for 45 min without clamping the renal artery. These mice were anesthetized again with pentobarbital at post-IRI 1, 7, and 14 days before the blood and kidney tissues were collected. Blood was used for renal function measurements, whereas tissues were used for the observation of lesions and relevant tests. Serum creatinine (SCr) levels were measured using an SCr Colorimetric Assay Kit (Cat #ADS-W-FM034, AIDISHENG Biotech).

Evaluation of Lactylation-Related Gene Scores and Metabolic Activity

The input for computing LRG signature for both microarray data and scRNA-seq data was based on the list of LRGs provided in Table S1. For bulk microarray data, we used Gene Set Variation Analysis (GSVA) to quantify and compare the LRG signatures across conditions. In scRNA-seq data, we quantified the LRG scores using the "AUCell" algorithm and verified using the "AddModuleScore" from Seurat. "AUCell" determines whether the provided gene set is enriched in each cell type by calculating the area under the curve (AUC) based on the ranked expression of genes, whereas "AddModuleScore" computes a module score by comparing the average expression of the input gene set to that of the control gene sets. The threshold for determining whether the lactylation signature was active in a given cell was chosen using the *AUCell_exploreThresholds* function, and each cell type was assigned to a high- or low-lactylation AUCell group based on the threshold score. Metabolic pathway quantification of scRNA-seq data was performed using "scMetabolism" R package, which calculates multiple metabolic pathway activities at the single-cell level.[30]

Differential Expression and Functional Enrichment Analysis

Differential expression analysis for microarray datasets was performed using "limma" R package. For exploring the differentially expressed genes (DEGs) in each cell cluster across conditions, we performed pseudo-bulk differential analysis using the "DESeq2" R package (version 1.46.0). Wald and likelihood ratio tests were used to identify the DEGs across multiple groups for each cell type. Differential expression analysis was conducted using FindMarkers from Seurat

Table 1 Clinical Information of GEO Datasets

GEO Identifier	Platform	Sample	Treatment	Tissue	Sampling Time	Sample Size
GSE180420	GPL21103	Mus musculus	Bilateral ischemia reperfusion (control; short ischemia time = 23min; long ischemia time = 30min)	Kidney	Post-surgery 1day, 3 days, 14 days	n= 6 control n=2 IRI short 1d n=2 IRI short 3d n=2 IRI short 14d n=2 IRI long 1d n=2 IRI long 3d n=2 IRI long 14d
GSE22459	GPL570	Homo sapiens	KTx	Kidney allograft biopsies	1 year	n= 25 normal n=40 IFTA
GSE53605	GPL571	Homo sapiens	KTx	Kidney allograft biopsies	2 years	n= 18 normal n= 10 IFTA
GSE76882	GPL13158	Homo sapiens	KTx	Kidney allograft biopsies	1 year	n= 99 normal n= 81 IFTA
GSE21374	GPL570	Homo sapiens	KTx	Kidney allograft biopsies	1 to 31 years	NA

Abbreviations: GEO, Gene expression omnibus; IFTA, interstitial fibrosis and tubular atrophy; KTx, kidney transplantation.

https://doi.org/10.2147/JIR.S548708

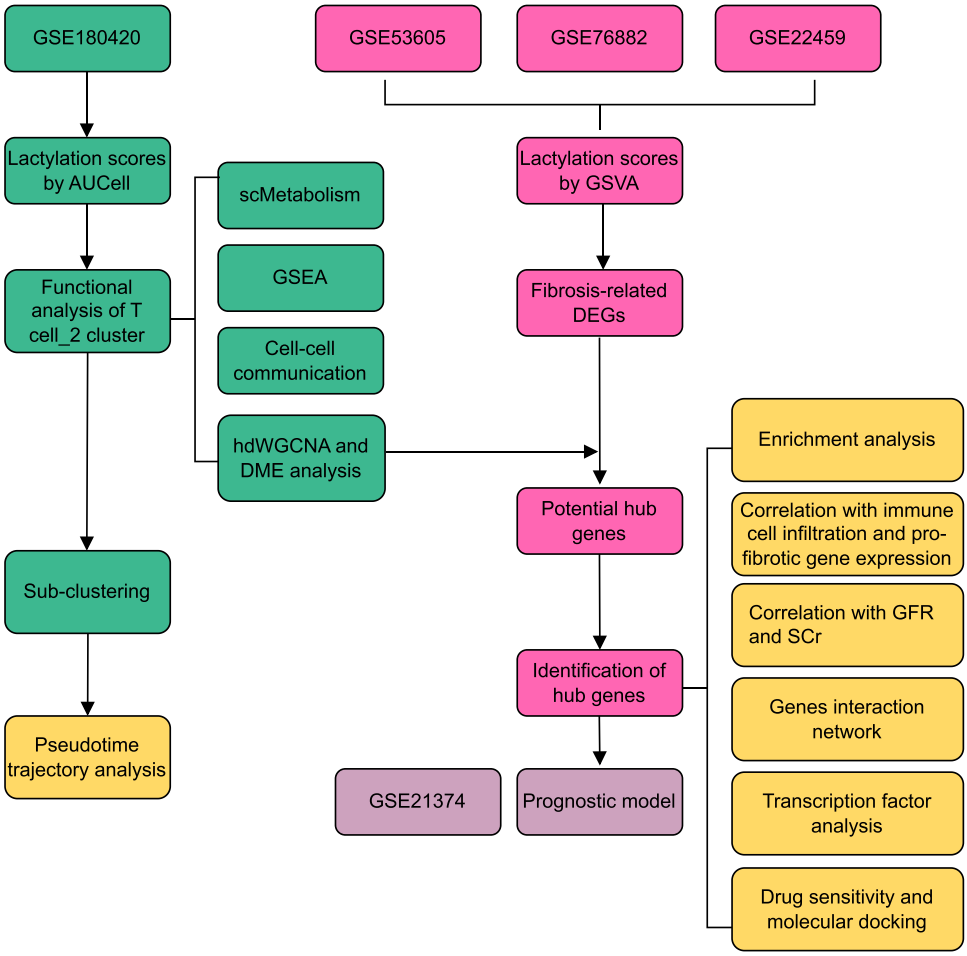

Figure 1 Workflow of the study.
Abbreviations: GSEA, gene set enrichment analysis; GSVA, gene set variation analysis; DEGs, differentially-expressed genes; hdWGCNA, high dimensional weighted gene co-expression network analysis; GFR, glomerular filtration rate; SCr, serum creatinine; DME, differential module eigengene.

to identify DEGs between the high- and low-lactylation groups. Significant DEGs were defined as false discovery rate (FDR) <0.05, and |log2FC| >1. Gene ontology (GO), Kyoto Encyclopedia of Genes and Genomes (KEGG), and gene set enrichment analyses (GSEA) were conducted using "clusterProfiler" (version 4.4.4). The false detection rate was <0.25 and the adjusted p value was <0.05.

Identification of Lactylation-Related Regulatory Hub Genes in the Key T Cell Subtype by hdWGCNA

To identify hub genes in the key T-cell subtype, we used hdWGCNA analysis,[31] an algorithm designed for single-cell data that constructs co-expression networks and assesses relationships with input features. We analyzed the associations between gene modules, ischemia time, and lactylation scores to identify gene modules closely related to key T cell clusters, lactylation enrichment, and repair. Furthermore, hub genes intersected with the DEGs obtained from the microarray data. The analyses followed the official hdWGCNA pipeline (https://smorabit.github.io/hdWGCNA/index.html). Briefly, scRNA-seq data were first converted to metacells using the MetacellsByGroups function. We then performed NormalizMetacells and ScaleData before computing eigengene-based connectivity (kME). We then conducted differential module eigengene analysis to identify modules that were up- or downregulated in a specified group of cells. Finally, module-trait association was analyzed using the GetModuleTraitCorrelation function.

https://doi.org/10.2147/JIR.S548708

Establishment of Lactylation-Related Risk Score Based on Machine Learning Algorithms

Machine learning has shown robust applicability in fitting predictive models to complex data or in identifying informative patterns within data.[32] To prove the diagnostic efficacy of the hub genes and to construct a robust diagnostic model, eight machine learning models were selected using the "Tidymodels" R package. The models include support vector machines (SVM), bagged neural networks via nnet, bagged trees, logistic regression, random forests, extreme gradient boosting (XGBoost), decision trees, and K-nearest neighbors. For tree-based methods, we reported either the number of trees or the tree depth depending on the algorithm. Specifically, the random forest model was constructed with 500 trees (engine = ranger), while the decision tree used a tree depth of 30 and a minimal node size of 2 (engine = rpart). The XGBoost model (engine = xgboost) was trained with 15 boosting iterations and a maximum tree depth of 6. For the neural network (engine = nnet), training was performed for 1000 epochs. The bagged tree model (engine = rpart) also adopted a tree depth of 30. The remaining classifiers—logistic regression (engine = glmnet), support vector machine (engine = kernlab), and k-nearest neighbor (engine = kknn) - were tuned based on their default hyperparameters. The combined microarray dataset, containing 131 IFTA samples and 142 normal samples, was randomly split into training (75%) and testing (25%) sets to prevent overfitting. The model training used a ten-fold cross validation to avoid bias due to imbalanced sample sizes, with 95% confidence interval (95% CI) computed using the standard error method. The evaluation parameters included the AUC for discrimination ability, accuracy for calibration, and Brier score for overall performance. Model with the highest AUC and lowest Brier score was considered to be optimal.

To construct a lactylation-related risk score, the GSE21374 dataset was randomly split into training and test sets in a 70:30 ratio.[33,34] Univariate Cox regression analysis was performed to screen for survival-related genes in the training set. Next, we used the least absolute shrinkage and selection operator (LASSO) to eliminate redundant genes and subjected the remaining potential genes to multivariate Cox regression analysis. We filtered for significant model genes (HR = 1, $p < 0.05$). Finally, we established a lactylation-related risk score using the formula: $\sum_{i=1}^{n} \beta i * \exp(i)$, where "exp" representing each gene's expression and βi represents the LASSO coefficient. Patients were categorized into high- or low-risk groups based on the median lactylation-related risk score. All analyses were performed using the "glmnet" R package. Kaplan-Meier survival plots, risk plots, and time-dependent ROC curves were generated to visualize survival differences and predict patient survival at 1, 3, and 5-years post-transplantation. Additionally, we applied the "Mime" R package[35] to the same dataset for selection of prognostic models and prognostic genes associated with graft outcomes, using ten machine learning algorithms and combinations. For external validation, we assessed the diagnostic value of hub genes in the combined microarray dataset and validated their expression in GSE53605, GSE76882, and GSE22459 datasets. The 95% CI was computed using 2000 stratified bootstrap replicates.

Estimation of Immune Cell Infiltration and Clinical Significance

Immune cell infiltration was assessed using two algorithms, including single-sample gene set enrichment analysis (ssGSEA) by "gsva" R package and CIBERSORT by "IOBR" R package[36] in the microarray data. The Nephroseq v5 database (http://v5.nephroseq.org/) is a comprehensive online platform that allows exploration of gene expression profiles in relation to the clinical parameters of kidney diseases. We investigated the correlation between hub gene expression levels and kidney function parameters, specifically the glomerular filtration rate (GFR) calculated using the Modification of Diet in Renal Disease (MDRD) formula, and serum creatinine levels in kidney transplant patients.

Ligand-Receptor Interactions, Pseudotime Trajectory Inference, and Gene Regulatory Network Analysis

The "CellChat" R package (version 2.1.2) was used to investigate cell-cell interactions and altered signaling pathways between short IRI and long IRI-treated samples in accordance with the vignette provided by the author.

We performed a pseudotime analysis of the key T cell subtypes and examined hub gene expression along the trajectory using the "monocle3" R package (version 1.3.7). For clustering and trajectory analysis, we first reduced the

dimensionality using UMAP and applied the "cluster_cells" function. We then determined the starting point of the trajectory based on the post-surgery time points (control, IRI 1d, IRI 3d, and IRI 14d).

Protein-protein interactions and their core functions were analyzed using the "GeneMANIA" database (https://genemania.org/). To understand the regulatory mechanisms of the 4 hub genes, we utilized "RcisTarget" R package (version 1.26.0) to identify their transcription factor (TF) and transcription factor binding motifs (TFBS) based on gene-motif rankings.[37] The Homo sapiens database was downloaded from the official website (https://resources.aertslab.org/cistarget/databases/homo_sapiens/hg38/refseq_r80/mc_v10_clust/gene_based/), which contains motif information 10kb around the transcription start site (TSS).

Drug Sensitivity Prediction and Molecular Docking Simulation

We predicted the potential target drugs (approved by FDA and those in clinical trial) using "CellMiner" database.[38] For each gene, we selected the top three drugs that showed the strongest correlations, and validated them through molecular docking. We obtained protein structures for the three target genes from the RCSB Protein Data Bank (https://www.rcsb.org/) and AlphaFold Protein Structure Database (https://alphafold.ebi.ac.uk/), and modified them using PyMOL 2.5.8 and AutoDockTools 1.5.7. AutoDock Vina was used to predict the binding affinities between the ligands and receptors.

RT-PCR, Immunohistochemistry, and Masson Trichrome Staining

The primer sequences are presented in Table 2. The RT-PCR process consisted of total RNA samples from the IRI kidney isolated using the SteadyPure Universal RNA Extraction Kit (Accurate Biotechnology Co., Ltd., Hunan, China), following the manufacturer's instructions. For qPCR analysis, RNAs was reverse-transcribed to cDNA using the Evo M-MLV RT Mix kit (Accurate Biotechnology Co., Ltd., Hunan, China). PCR was conducted using a Real-time PCR detection system (Applied Biosystems, USA) with a SYBR Green Pro Taq HS qPCR kit (Accurate Biotechnology Co., Ltd., Hunan, China). The data were normalized to GAPDH expression and relative quantification was performed using the 2-ΔΔCt method.

To observe morphological changes, renal tissues were preserved in 10% paraformaldehyde and embedded in paraffin. Tissue slices were then deparaffinized, rehydrated, and subjected to hematoxylin and eosin (H&E) and Masson trichrome staining. For immunohistochemical staining, different types of primary antibodies, such as anti-CD3 and anti-CD45, were used during the first overnight incubation, followed by incubation with the appropriate secondary antibodies.

Statistical Analysis

All statistical analyses were performed using R software (version 4.2.1). The Wilcoxon rank-sum test and Kruskal–Wallis test was used for comparisons between two groups and among multiple groups, respectively. Pearson's correlation analysis was used to assess the relationships between variables. Variance inflation factor (VIF) was used to assess multicollinearity. Statistical significance was considered at (, * $p<0.05$, ** $p<0.01$, *** $p<0.001$). All p-values were adjusted using FDR unless stated otherwise.

Table 2 Genes and Primer Sequences

Gene	Primer Sequences
H2-T23 (mouse)	Forward: 5'-GGACCGCGAATGACATAGC-3'
	Reverse: 3'-GCACCTCAGGGTGACTTCAT-5'
Coro1a (mouse)	Forward: 5'-AAGGCAGAGCAGATGGGATG-3'
	Reverse: 3'-CCAAGTGGTTTGTGAGACGC-5'
Tuba1a (mouse)	Forward: 5'-TGCCTTTGTGCACTGGTATG-3'
	Reverse: 3'-CTGGAGCAGTTGACGACAC-5'
Ighm (mouse)	Forward: 5'- GACAAGTCCACTGGTAAACCC-3'
	Reverse: 3'-CCGCCTGTGTCAGACATGA-5'

https://doi.org/10.2147/JIR.S548708

Results

A T Cell Subpopulation Exhibited Enhanced Lactylation Levels

To investigate the role of lactylation in fibrosis, we first analyzed the lactylation enrichment scores of the IFTA and control groups. Batch effects were successfully mitigated, as evidenced by the sample distributions showing improved consistency in the PCA plots (Figure S1). The IFTA group had higher lactylation scores than the other groups (Figure 2A). Furthermore, overall lactylation scores after IRI showed enhanced enrichment compared to the control across the majority of cell types by

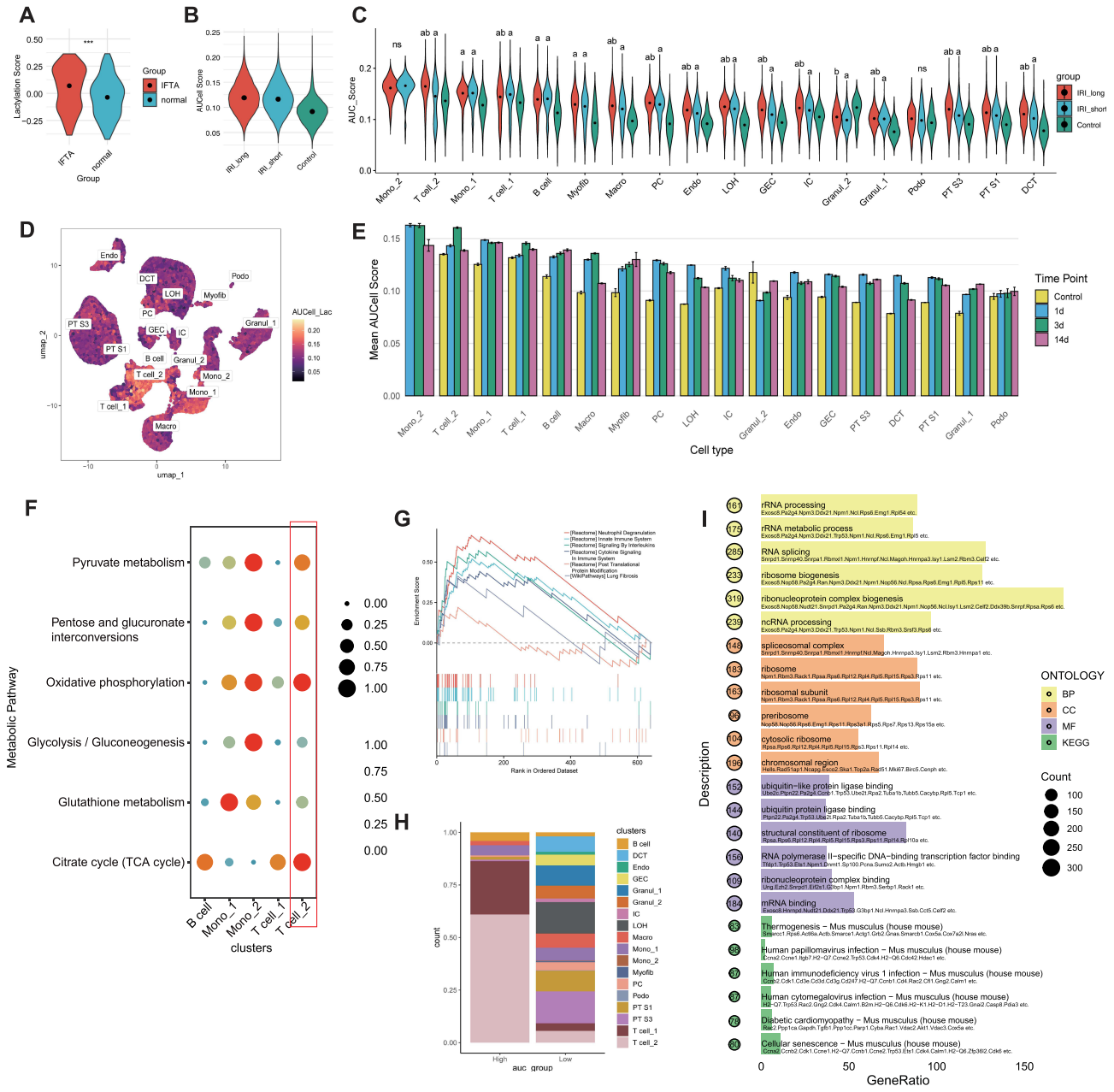

Figure 2 Identification of a T cell subset characterized by elevated lactylation activity. (**A**) Violin plot displaying lactylation activity by GSVA in IFTA samples. (**B** and **C**) AUCell scores of lactylation activity across different ischemia groups and cell types. (**D**) Feature plot illustrating overall lactylation activity across all cell types. (**E**) Mean AUCell scores of lactylation across cell types across at different time points before and after IRI, in descending order. (**F**) Bubble plot showing metabolic pathway enrichment in the top five lactylation-activated cell types. (**G**) GSEA analysis of pseudobulk-DEGs in T cell_2 cluster. (**H**) Changes in cell proportion between high lactylation and low lactylation groups. (**I**) GO/ KEGG enrichment analysis of DEGs between high and low lactylation groups. a, $p < 0.05$, as compared to the Control group; b, $p < 0.05$, as compared to the IRI_short group; ns, not significant; ***, p<0.001.

Abbreviations: GSEA, gene set enrichment analysis; GSVA, gene set variation analysis; DEGs, differentially-expressed genes; IFTA, interstitial fibrosis and tubular atrophy; GO, gene ontology; KEGG, Kyoto Encyclopedia of Genes and Genomes.

both AUCell and AddModuleScore analyses (Figure 2B and C; Figure S2). Since long ischemia time is associated with maladaptive repair, while short ischemia is established as regeneration,[22] we also examined the lactylation levels among different ischemia duration groups. The long ischemia group exhibited elevated lactylation levels compared to both the short ischemia and normal groups, a trend persisting up to 14 days after surgery, suggesting a potential role of lactylation in the maladaptive repair process (Figure S3). Notably, the T cell_2 cluster showed the highest lactylation score and increased lactylation in the long ischemia group compared to that in the short ischemia group (Figure 2D–E). Given the close relationship between lactylation and metabolic reprogramming, we assessed the metabolic activities across cell types. We found upregulated glycolysis and TCA cycle activity in the T cell_2 cluster, indicating potential metabolic reprogramming, along with higher lactylation levels (Figure 2F). Further enrichment analysis using GSEA confirmed potential post-translational protein modifications, lung fibrosis, cytokine signaling, and neutrophil degranulation functions in the T cell_2 subset (Figure 2G; Table S2). The lactylation threshold was set to 0.207. By categorizing the cell types into high- and low-lactylation active groups, we discovered a significant increase in the proportion of T cell_2 and T cell_1 clusters (Figure 2H). The lactylation-active cell groups showed upregulated RNA metabolism, ribosome regulation, ubiquitin protein ligase binding, viral infection, and cellular senescence (Figure 2I).

T Cell_2 Cluster Showed Enhanced Cell-Cell Communication with Monocyte-Macrophages and Identification of T Cell_2 Lactylation Related Genes by hdWGCNA

To elucidate changes in cell-cell interactions during the maladaptive process, cell-cell communication analysis was performed and compared between the short and long ischemia time groups. This analysis revealed an increased number of interactions between the T cell_2 cluster and a subset of monocytes (Figure 3A). Altered global signaling pathways indicated the upregulation of pro-inflammatory and pro-fibrotic pathways, including tumor necrosis factor (TNF), transforming growth factor beta (TGFβ), macrophage migration inhibitory factor (MIF), C-C motif chemokine ligand (CCL), complement, fibroblast growth factor (FGF), and TNF superfamily member 12 (TWEAK) (Figure 3B). Specifically, the MIF-(CD74 +CD44) and CCL6-CCR2 ligand-receptors emerged as the prominent activated modes of interaction between T cell_2 clusters and monocytes, while MIF-(CD74+CXCR4) was significantly activated between T cell_2 clusters and B cells and macrophages (Figure 3C). hdWGCNA was used to identify hub genes in the T cell_2 cluster. After setting the soft threshold to 7, a co-expression network was constructed, which revealed 10 eigengene modules (Figure 3D–F). Differential module eigengene analysis (DME) showed that seven gene modules were upregulated in the long ischemia group, with each module enriched in distinctive biological processes (Figure 3G and H). Overall, modules M2, M4, and M6 showed relative specificity to the T cell_2 cluster and were positively associated with higher lactylation AUCell scores and longer ischemia time (Figure 3F–I). The top 25 genes contributing to each module included Laptm5, H2-T23, Rpl, Rbm3, and Sumo2 (Figure 3J). Lastly, we intersected LRGs using hdWGCNA from the T cell_2 cluster and fibrosis-related DEGs obtained from microarray data, resulting in 38 hub genes (Figure 3K; Tables S3–4).

Validation of Lactylation-Related Hub Genes as Diagnostic Markers for Allograft Fibrosis and Development of a Predictive Risk Score for Graft Survival

Among the eight machine learning algorithms tested, random forest emerged as the optimal model, achieving an AUC of 0.888, Brier score of 0.140, accuracy of 0.804 in the training set (Figure 4A), and an AUC of 0.897 in the test set (Figure 4B), with cutoff being 0.579 (Table S5). The other two top performing models were the bagged neural network model, achieving an AUC of 0.861 and a Brier score of 0.176, while the bagged tree model had an AUC of 0.859 and a Brier score of 0.160 (Figure 4A and B; Table S5).

Univariate Cox regression analysis showed that 31 genes correlated with graft survival before LASSO regression, and multivariate Cox regression selected four genes (TUBA1A, CORO1A, HLA-E, and IGHM) to be significantly associated with graft status (Figure 4C–F). The risk score was calculated as follows: risk score = 1.568*exp(TUBA1A) + (−1.921) *exp(CORO1A) + 3.458*exp(HLA-E) + 0.504*exp(IGHM). The risk plot showed that the risk group efficiently predicted the graft function status (Figure 4G). In the training dataset, time-dependent ROC curves demonstrated the

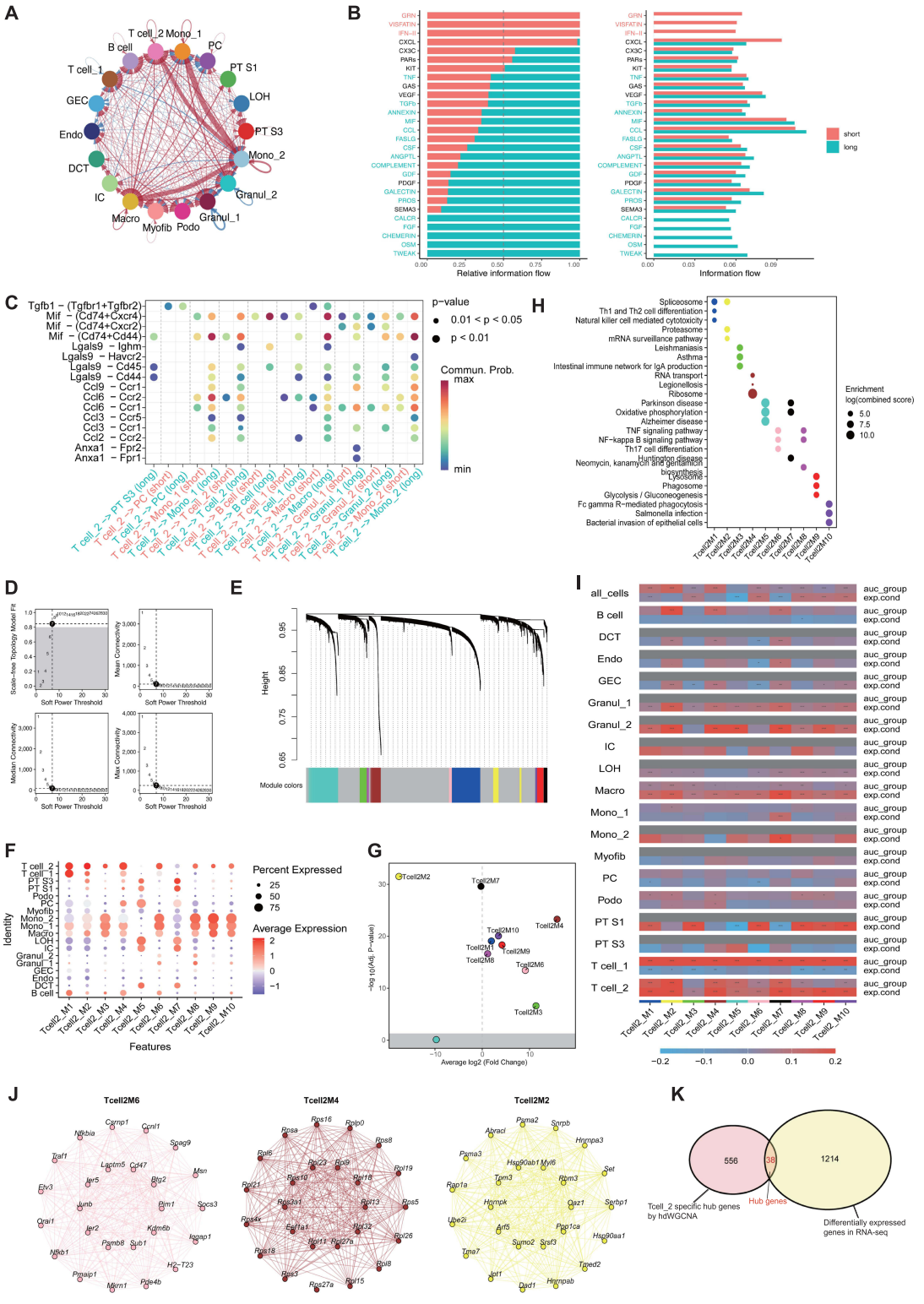

Figure 3 Identification of cell-specific hub genes and cell-cell communication analysis. (**A**) Differential number of interactions in long ischemia group compared to short ischemia group. (**B**) Significant altered signaling pathway activity between short and long ischemia conditions. (**C**) Enhanced outgoing signaling of ligand–receptor interactions from the T cell_2 cluster in long IRI, compared to short IRI by bubble plot. (**D**) Optimal soft threshold selection. (**E**) Dendrogram of T cell_2 cluster colored by modules. (**F**) Dot plot visualizing different module gene expressions in cell clusters. (**G**) Volcano plot showing fold-change and significance level of DME analysis. (**H**) KEGG analysis for each module. (**I**) Heatmap of module-trait correlation. (**J**) Module network plots visualizing the top 25 hub genes within the key modules. (**K**) Intersection of hub genes and fibrosis-related DEGs. *, p<0.05; **, p<0.01; ***, p<0.001.

Abbreviations: KEGG, Kyoto Encyclopedia of Genes and Genomes; DEGs, differentially-expressed genes; DME, differential module eigengene; exp.cond, experimental conditions; auc_group, groups based on the lactylation AUCell scores.

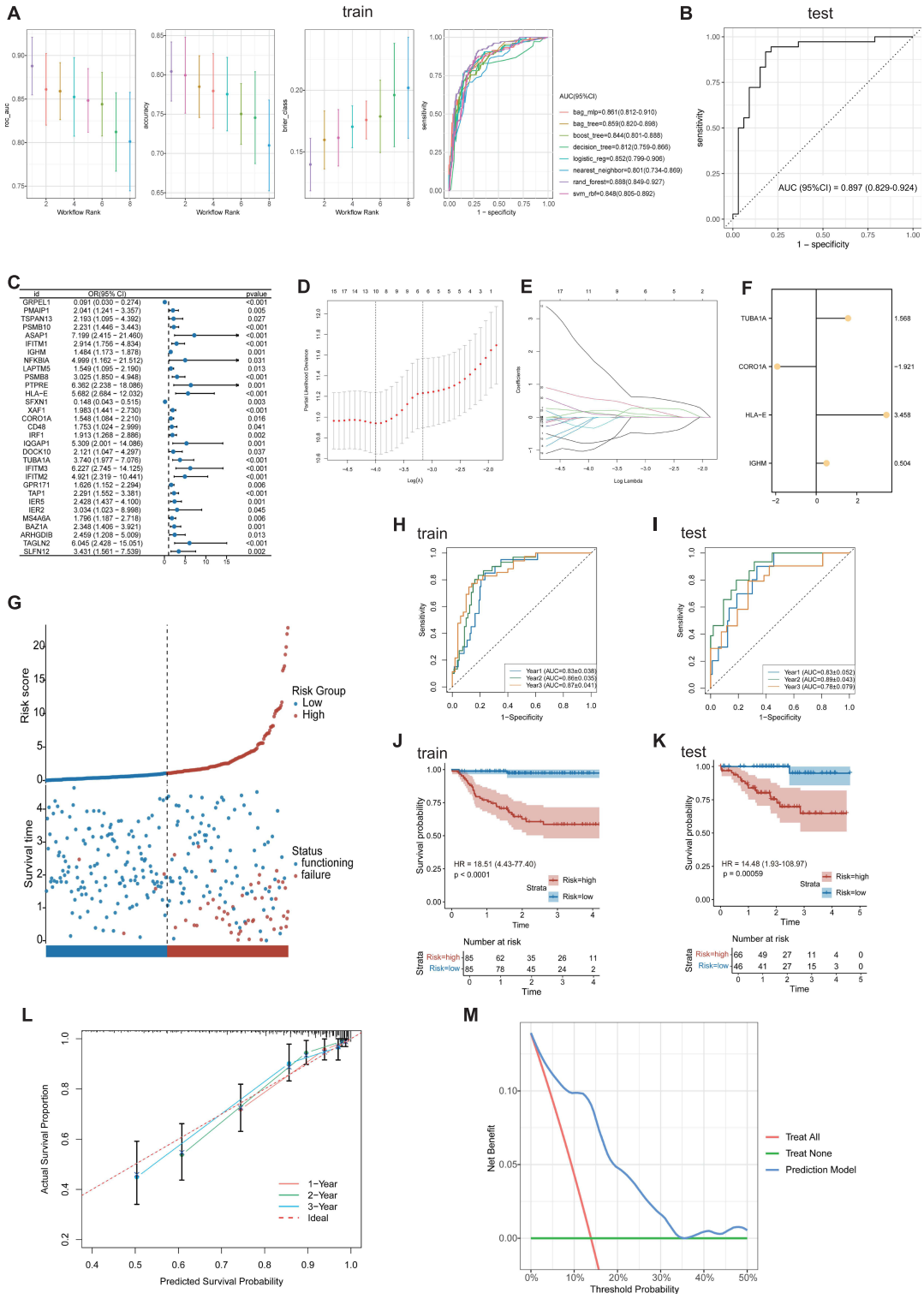

Figure 4 Construction of lactylation-related risk score. (**A** and **B**) Comparison of the eight machine learning algorithms in the train set, and validated in the test set using random forest model. (**C**) Univariate regression analysis of the model genes in the GSE21374 cohort. (**D** and **E**) Regularization path and coefficient path in the LASSO model. (**F**) Lollipop plot depicting multivariate regression analysis generated the final four hub genes. (**G**) Risk map of graft survival status between high and low risk group. (**H** and **I**) ROC curve of the risk group in predicting 1-, 2-, and 3- year graft survival in train and test set, respectively. (**J** and **K**) K-M curve of the high and low risk groups in train and test set, respectively. (**L**) Calibration plot of the prognostic model. (**M**) DCA plot of the prognostic model.

Abbreviations: rand_forest, random forest; bag_mlp, bagged neural networks; bag_tree, bagged trees; logistic_reg, logistic regression; svm_rbf, support vector machines; boost_tree, extreme gradient boosting; decision_tree, decision trees; nearest_neighbor, K-nearest neighbors; AUC, area under curve; ROC, receiver operating characteristic curve; LASSO, least absolute shrinkage and selection operator; 95% CI, 95% confidence interval.

https://doi.org/10.2147/JIR.S548708

robustness of the risk score in predicting graft survival rates at one year (AUC = 0.83), two years (AUC = 0.86), and three years (AUC = 0.87). In the test set, the AUCs were 0.83, 0.89, and 0.78 for 1-,2-, and 3-years graft survival, respectively (Figure 4H and I). K-M curves revealed statistically significant differences in survival probability between the low- and high-risk groups (Figure 4J and K). In the training group, the hazard ratio (HR) was 18.51 ($p < 0.0001$), whereas in the test group, the HR was 14.48 ($p = 0.00059$). Furthermore, calibration curves and decision curve analysis (DCA) verified the clinical utility and reliability of the model (Figure 4L and M). Notably, machine learning-based gene selection also ranked the four hub genes among the top ten predictors of graft outcomes (Figure S4). Collectively, these findings highlight the robust predictive power and translational potential of the proposed prognostic model.

The expression of these four hub genes was upregulated in the GSE22359, GSE53605, and GSE76882 datasets. The diagnostic value of each gene was also validated in the combined dataset, with each showing robust diagnostic efficacy and an AUC ranging from 0.776 to 0.859. The IFTA group had a higher risk score than the normal group (Figure 5A–C). The four hub genes were positively correlated with each other and were enriched in biological processes, including antigen binding, lymphocyte-mediated immunity, lymphocyte activation, peptidoglycan binding, and apoptosis, as evidenced by the gene-gene interaction network and GO/KEGG enrichment analyses (Figure 5D–F). All VIF values of the four genes were below 5, indicating weak potential of multicollinearity (Figure S5). To examine the potential downstream effects of hub genes, we analyzed their correlation with pro-fibrotic gene expression, which showed moderate associations (Figure 5G). Moreover, the infiltration of immune cells showed varied associations with the core genes. Generally, hub gene expression and risk score were positively correlated with B cells, macrophages, T helper cells, and cytotoxic cells, whereas negatively associated Treg findings were validated by ssGSEA and CIBERSORT algorithms (Figure 5H and I). In summary, we found that four lactylation-related genes in the T cell_2 cluster effectively distinguished kidney allograft fibrosis and predicted the graft survival.

To evaluate the clinical significance of the identified hub genes, we examined their associations with kidney function parameters in allograft biopsies (Figure 6). CORO1A, HLA-E, and IGHM expression levels showed a strong negative correlation with estimated GFR and a positive correlation with serum creatinine (SCr) (Figure 6A–F). TUBA1A expression displayed a moderate association with impaired kidney function (Figure 6G and H). Collectively, these findings indicate that elevated expression of these hub genes is linked to deteriorated allograft function.

Sub-Clustering and Pseudotime Trajectory Analysis of the Key T Cell Cluster

We verified hub gene expression in the scRNA-seq dataset (Figure 7A). To capture the heterogeneity of key cell types, we sub-clustered the T cell_2 cluster. Initial quality control was performed with a mitochondrial percentage <20% (Figure S6). Following the removal of myeloid-mixed cells, we reanalyzed the T cell_2 cluster using dimensionality reduction and clustering. This yielded 11 cell clusters annotated based on canonical T-lymphocyte markers (Table S6). Based on the top 10 expressed genes for each cell cluster, we further annotated these clusters into eight functionally distinct cell types (Figure 7B and C): 834 naïve T cells (Ccr7, Lef1), 430 activated Th17 (Rora, Tnfrsf4, Icos), 203 proliferative T cells (Gm10260, Kap), 474 NK T (Tyrobp, Ccl5, Nkg7), 342 metabolic adaptive T cells (Gpx3, Aldob, Mt1), 97 γδ T (Tcrg-C1), 75 macrophages (C1qb, Cd74, C1qa), and 84 un-classified cells (Calca, Lmo4). These cell types exhibited marked proportional changes between the control and IRI groups, with a significant decrease in the proportion of proliferative T cells and an increased percentage of activated Th17 and γδ T cells (Figure 7D). Notably, we discovered enhanced lactylation activity in naïve T cells, activated Th17 cells, NK T cells, and γδ T cells, while Mif expression was predominantly expressed in metabolic adaptive T cells, with other cell types moderately expressing Mif (Figure 7E). H2-T23 (HLA-E gene symbol for Mus musculus), Ighm, Tuba1a, and Coro1a appeared to be generally expressed in naïve T cells, NK T cells, and activated Th17 cells (Figure 7F). Subsequent pseudotime trajectory inference showed naïve T cells at the beginning of the developmental trajectory and NK T cells and activated Th17 cells at the middle and end of the trajectory (Figure 7G). Concurrently, we observed a gradual increase in the expression of the four hub genes during the middle and later stages of the trajectory, although the expression of Ighm and Tuba1a was marginal (Figure 7H).

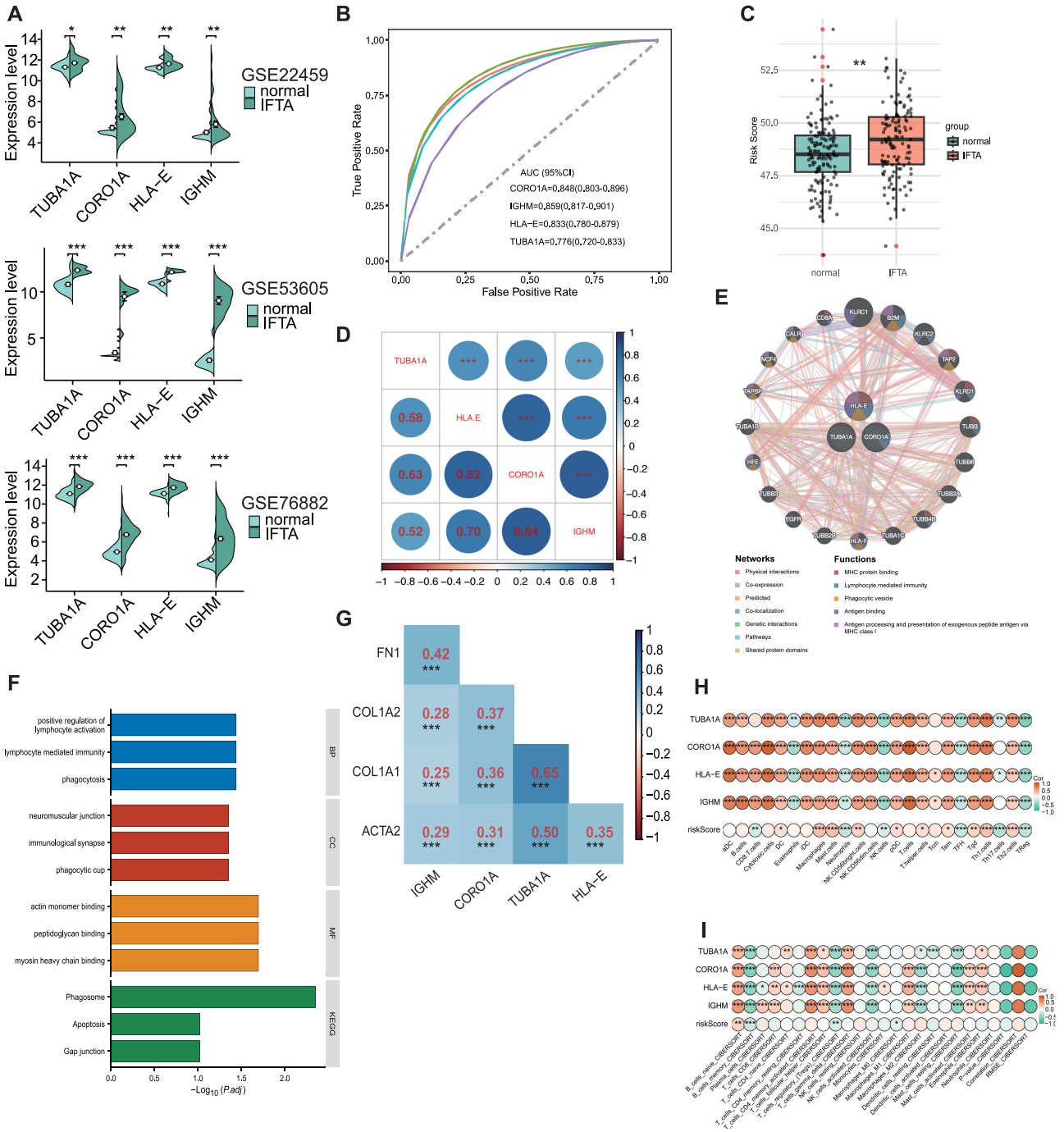

Figure 5 Validation and functional analysis of the hub genes. (**A**) Expression levels of the hub genes between control and IFTA samples. (**B**) ROC curves for each hub genes in distinguishing IFTA from normal samples. (**C**) Comparison of the risk score in control and IFTA samples. (**D**) Heatmap showing the correlation matrix among hub genes. (**E**) Gene-gene interaction network of the hub genes. (**F**) Bar plot of the enrichment analysis of the key genes. (**G**) Correlation between hub genes and established pro-fibrotic gene expression levels. (**H** and **I**) Bubble plots of the relationship between immune cell infiltration, risk score, and model genes using ssGSEA and CIBERSORT algorithms, respectively. 95% CI, 95% confidence interval; *, p<0.05; **, p<0.01; ***, p<0.001.

Abbreviations: ROC, receiver operating characteristic curve; AUC, area under the curve; IFTA, interstitial fibrosis and tubular atrophy; BP, biological process; CC, cellular component; MF, molecular function; KEGG, Kyoto Encyclopedia of Genes and Genomes.

Transcriptional Regulation and Potential Therapeutic Analyses

Using RcisTarget, we analyzed the TF and TFBS for three of the four hub genes (IGHM was not documented in the database). Our analysis showed that RFX3/SRF regulates HLA-E and CORO1A, whereas ZNF791 regulates CORO1A and TUBA1A (Figure 8A and B). Drug sensitivity analysis showed significant positive correlations between specific genes and drugs.

https://doi.org/10.2147/JIR.S548708

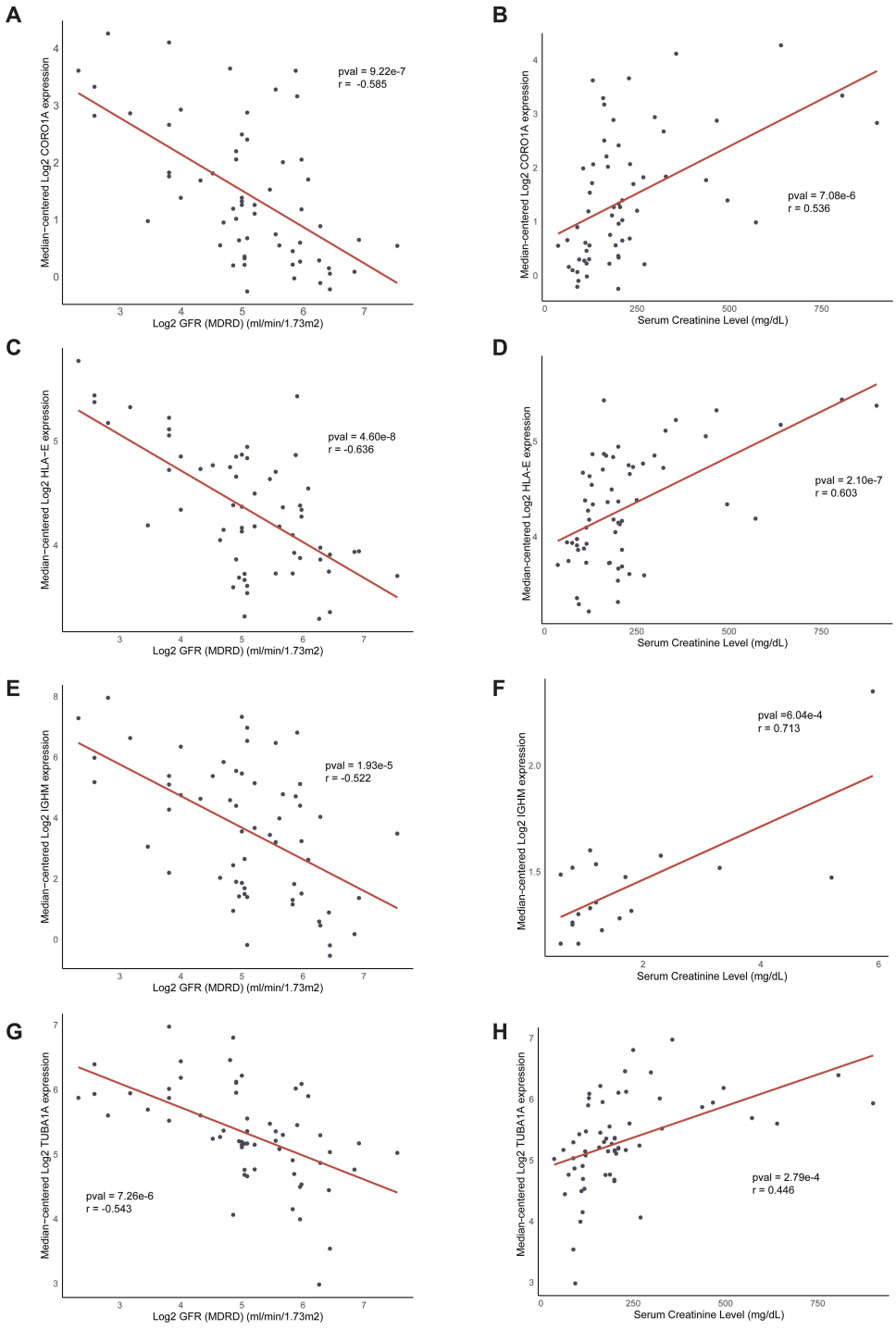

Figure 6 Correlation between hub gene expression levels and kidney function. Pearson correlation analysis was performed to assess the relationship between the median-centered log2-transformed expression levels of (**A** and **B**) CORO1A, (**C** and **D**) HLA-E, (**E** and **F**) IGHM, and (**G** and **H**) TUBA1A and log2-transformed GFR and serum creatinine levels, respectively.

Abbreviations: GFR, glomerular filtration rate; r, Pearson correlation coefficient; pval, adjusted p value.

TUBA1A was positively correlated with LY-294002, floxuridine, and GSK-2126458 (omipalisib) (Figure 8C–E); CORO1A showed high sensitivity to nelarabine, carmustine, and ST-3595 (Figure 8F–H), while HLA-E showed positive sensitivity to PLX-4720, CUDC-427, and vemurafenib (Figure 8I–K). The binding affinity of each pair was validated using molecular docking analysis (Figure 9). The binding affinity for HLA-E were the highest, with PLX-4720 −8.4 kcal/mol, CUDC-427 −8.2

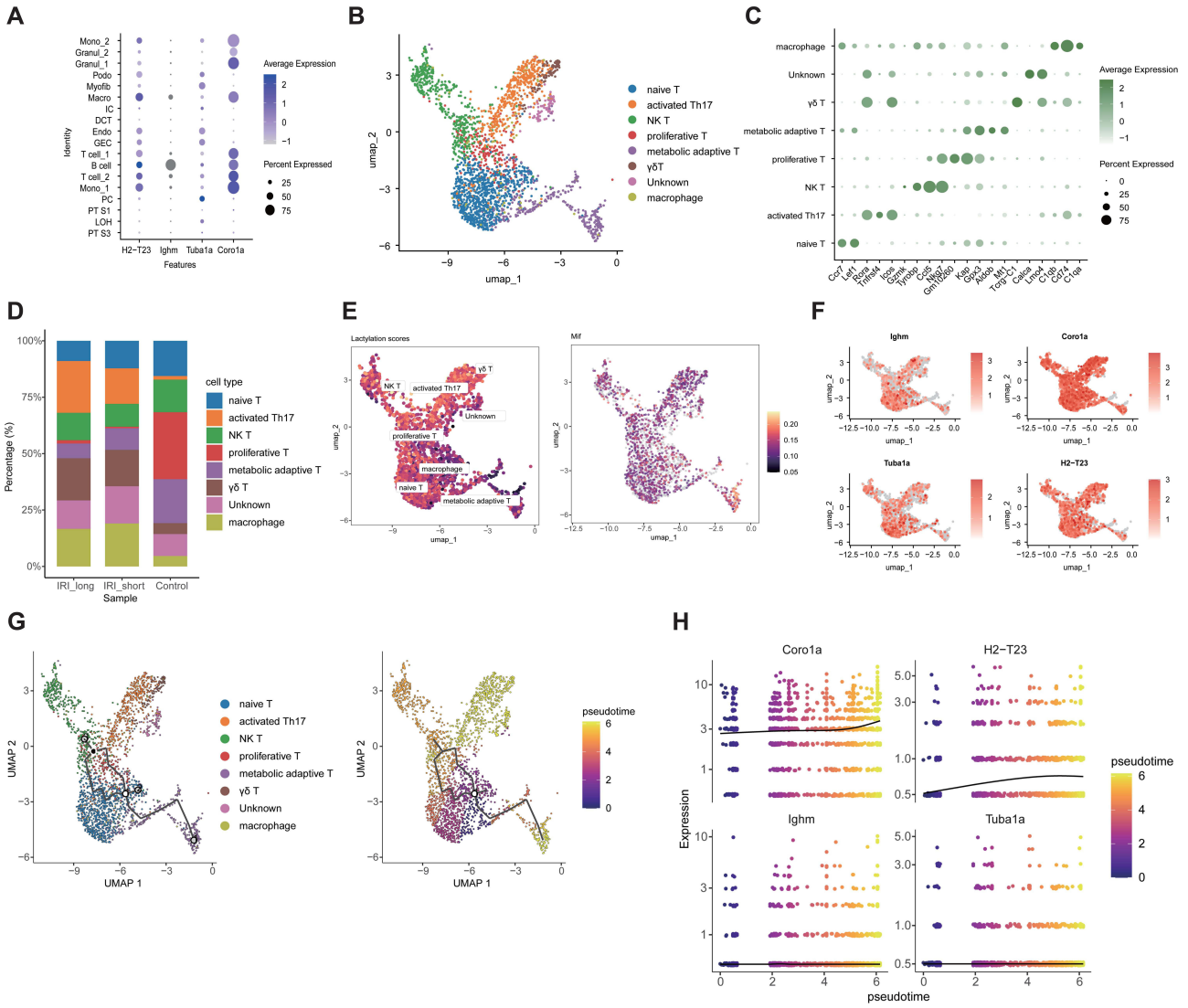

Figure 7 Pseudotime trajectory analysis of hub genes. (**A**) Dot plot showing the expression patterns of hub genes across samples in the GSE180420 dataset. (**B**) UMAP visualization of 8 sub-clusters derived from the sub-clustering of T cell_2 populations. (**C**) Dot plot highlighting the expression of distinct cell type markers across 8 identified cell types. (**D**) Bar plot of the differences in cell proportions in sham, short-ischemia time, and long-ischemia time. (**E**) Feature plot showing the distribution of lactylation-related scores and MIF expression. (**F**) Feature plots demonstrating the expression of hub genes. (**G**) UMAP visualization after dimensionality reduction, with cells clustered according to time points after ischemia using Monocle. (**H**) Gene expression dynamics along pseudotime.
Abbreviation: UMAP, manifold approximation and projection.

kcal/mol, and vemurafenib −9.4 kcal/mol (Figure 9A–C). For CORO1A, nelarabine and ST-3595 showed high binding affinity, with the binding energy being −7.9 kcal/mol and −8.1 kcal/mol, respectively, while carmustine only showed weak to moderate binding affinity (Figure 9D–F). Lastly, floxuridine (−7.3 kcal/mol), GSK-2126458 (−8.5 kcal/mol), and LY-294002 (−7.5 kcal/mol) also showed robust affinity to TUBA1A (Figure 9G and I).

Laboratory Validation of the Four Hub Genes in a Unilateral Ischemia-Reperfusion Injury Mouse Model

Histological analysis of the kidney tissues following IRI revealed significant structural changes. H&E staining showed tubular disorganization along with pronounced immune cell infiltration, whereas Masson's trichrome staining confirmed substantial interstitial fibrosis at 7 and 14 days post-IRI (Figure 10A; Additional File 1). Moreover, IHC staining for CD45, a pan-immune cell marker, and CD3, a T cell-specific marker, showed upregulated expression after IRI, which became especially pronounced in the long-term after IRI (Figure 10A). Due to the normal function of the contralateral

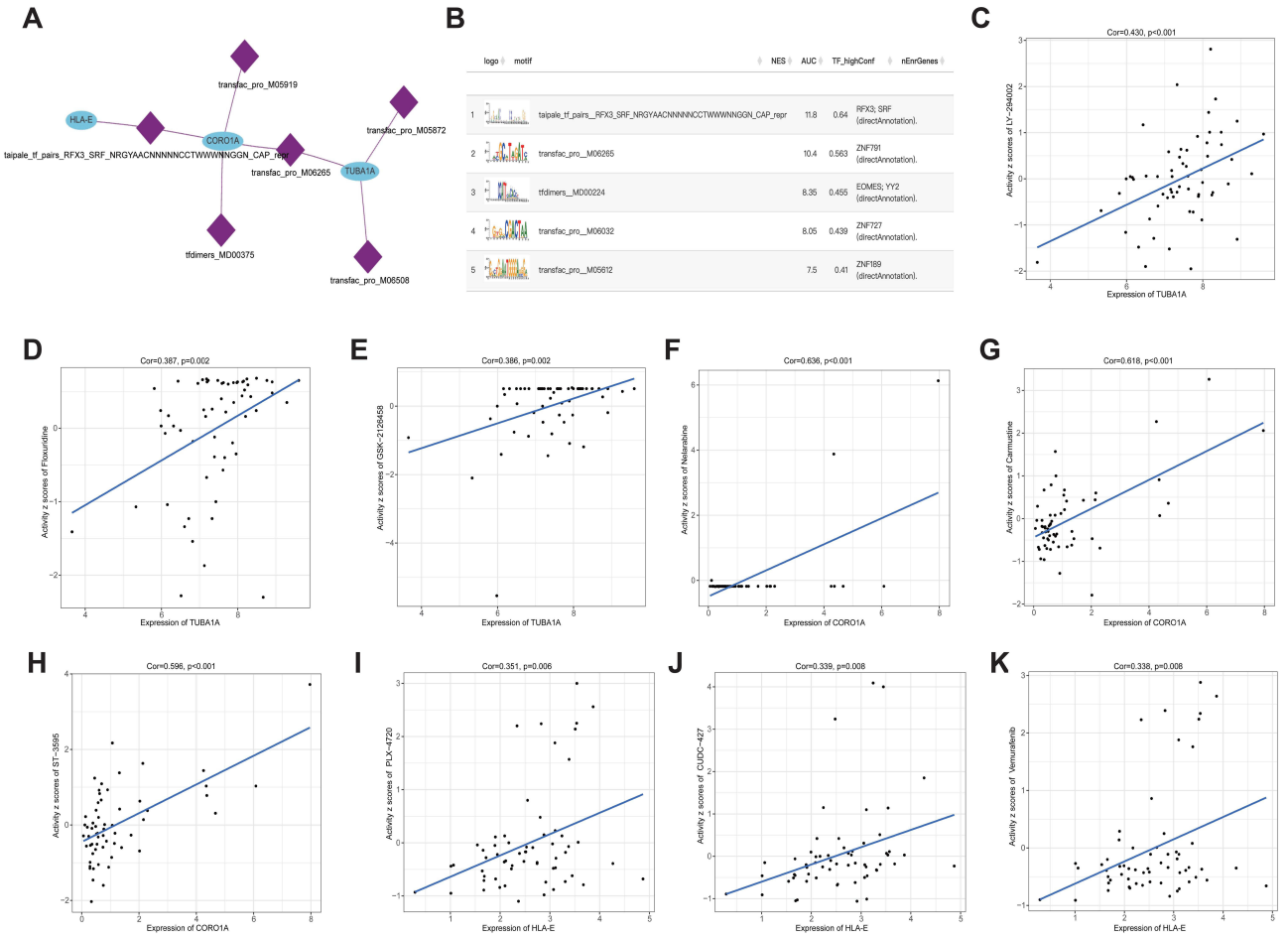

Figure 8 Transcription factor and drug sensitivity analysis. (**A** and **B**) Transcription factor and transcription factor binding motifs by ranking. Scatter plots depicting the correlation between the expression levels of (**C**–**E**) TUBA1A, (**F**–**H**) CORO1A, (**I**–**K**) HLA-E and the activity (*z* scores) of the three most highly correlated drugs, respectively.
Abbreviations: NES, normalized enrichment scores; Cor, Pearson correlation coefficient.

kidney, SCr levels exhibited a transient elevation on the first day post-IRI but remained within the normal range at 7 and 14 days after IRI (Figure 10B). Consistently, the expression levels of the established fibrotic marker genes Fn1 and Acta2 were upregulated, supporting the presence of fibrosis, whereas the mRNA expression of hub genes (H2-T23, Tuba1a, Ighm, and Coro1a) was also significantly upregulated in the renal tissue of the IRI group ($p < 0.05$), particularly 7 days post-surgery, indicating their long-term involvement in IRI-induced fibrogenesis (Figure 10C).

Discussion

In this study, we identified genes from a T cell subpopulation characterized by high lactylation levels that effectively distinguished kidney allograft fibrosis and predicted graft survival. We verified their increased expression in a mouse model of unilateral IRI-induced fibrosis. Pathway enrichment analysis of the key T cell cluster and hub genes suggested their involvement in pro-inflammatory processes, ribosome regulation, and apoptosis. Based on the hub genes, we developed a prognostic risk score using multiple machine-learning models. Finally, potential pharmacological targets were identified and verified using molecular docking simulations.

Our analysis of lactylation scores in both IFTA and IRI samples revealed significantly elevated levels in IFTA allografts and after IRI, particularly in the long ischemia group, indicating a potentially critical role of lactylation in the fibrotic niche. These findings align with the existing literature showing that persistently elevated glycolysis, a condition that predisposes cells to lactylation, promotes AKI-to-CKD transition.[12,39] Our results suggest that inhibiting lactylation of key glycolytic enzymes could curb IRI.[40,41] However, the precise mechanism by which lactylation contributes to the

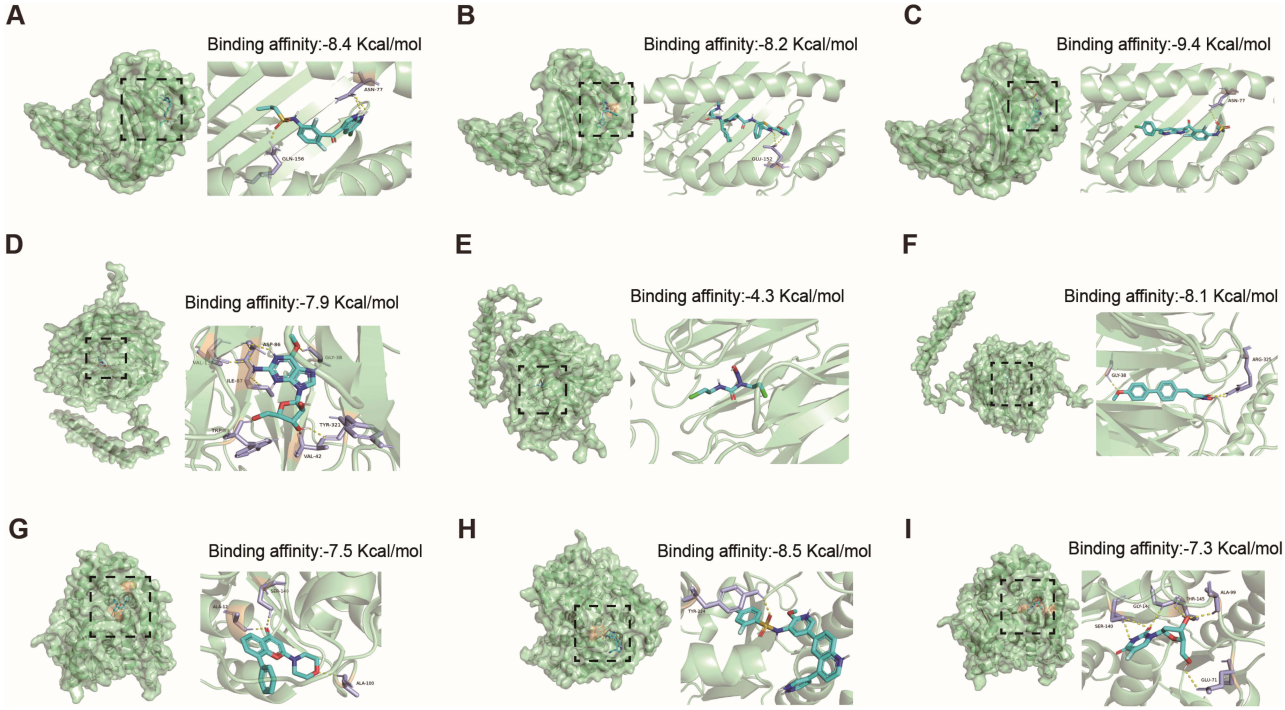

Figure 9 Molecular docking simulations. (**A**–**C**) Simulation of PLX-4720, CUDC-427, vemurafenib with HLA-E, respectively. (**D**–**F**) Simulation of nelarabine, carmustine, ST-3595 with CORO1A, respectively. (**G**–**I**) Simulation of LY-294002, GSK-2126458, floxuridine with TUBA1A, respectively. Black dotted lines indicate protein-drug interaction sites.

maladaptive repair remains unclear. Elevated lactate-related gene signatures and lactate-driven lactylation levels have been observed in models of lupus nephritis and diabetic nephropathy, both of which are characterized by kidney fibrosis.[13,42] Interestingly, some studies have suggested that lactylation may play a protective role following IRI. For example, histone lactylation upregulates reparative genes in macrophages and infiltrating monocytes following myocardial IRI, exerting anti-inflammatory and proangiogenic effects on cardiomyocytes.[43] Similarly, upregulation of lactylation in the c-Myc pathway, driven by increased glycolysis-generated lactate, may facilitate tubular epithelial cell proliferation and recovery post-IRI.[44]

Cellular analysis revealed elevated lactylation levels in a distinct T cell subcluster (T cell_2) compared to other cell types, with lactylation levels positively correlated with ischemia severity. This subpopulation of T cells exhibits metabolic reprogramming, marked by enhanced glycolysis, fibrosis, and post-translational modifications, along with a pro-inflammatory phenotype. Subsequent cell-cell communication identified upregulated interactions between the T cell_2 cluster and monocyte subsets, suggesting its potential role in amplifying early inflammatory responses or coordinating crosstalk among other immune cells. Collectively, these findings implicate lactylation within this T cell cluster as a potential driver of maladaptive repair following IRI.

Our findings are consistent with growing evidence demonstrating that upon antigen activation, T cells undergo rapid metabolic reprogramming, shifting toward oxidative phosphorylation and glycolysis as the dominant energy consumption modalities. This metabolic shift also activates the pentose phosphate pathway in cancer models and diseases characterized by hypoxia,[9,10,45] thus influencing the expression of key immune-related genes and T-cell functions.[46] A key regulator is LDHA, the glycolytic enzyme whose deletion in T cells reduced IFN-γ production.[47] Moreover, exogenous lactate has likewise shown to prime CD4+T cells to produce pro-inflammatory IL-17 while inhibiting CD4+/CD8+T cell motility mediated by Slc5a12 and Slc16a1 transporter proteins.[48] Consistently, we observed elevated lactylation scores in activated Th17 cells. Previous studies have highlighted their heterogeneity during metabolic reprogramming, with pathogenic Th17 subsets particularly enriched for glycolysis-related genes.[49] Moreover, pharmacological induction of hepatocyte-derived lactate by arsenic has shown to promote Th17 differentiation through interferon regulatory factor 4 lactylation, leading to

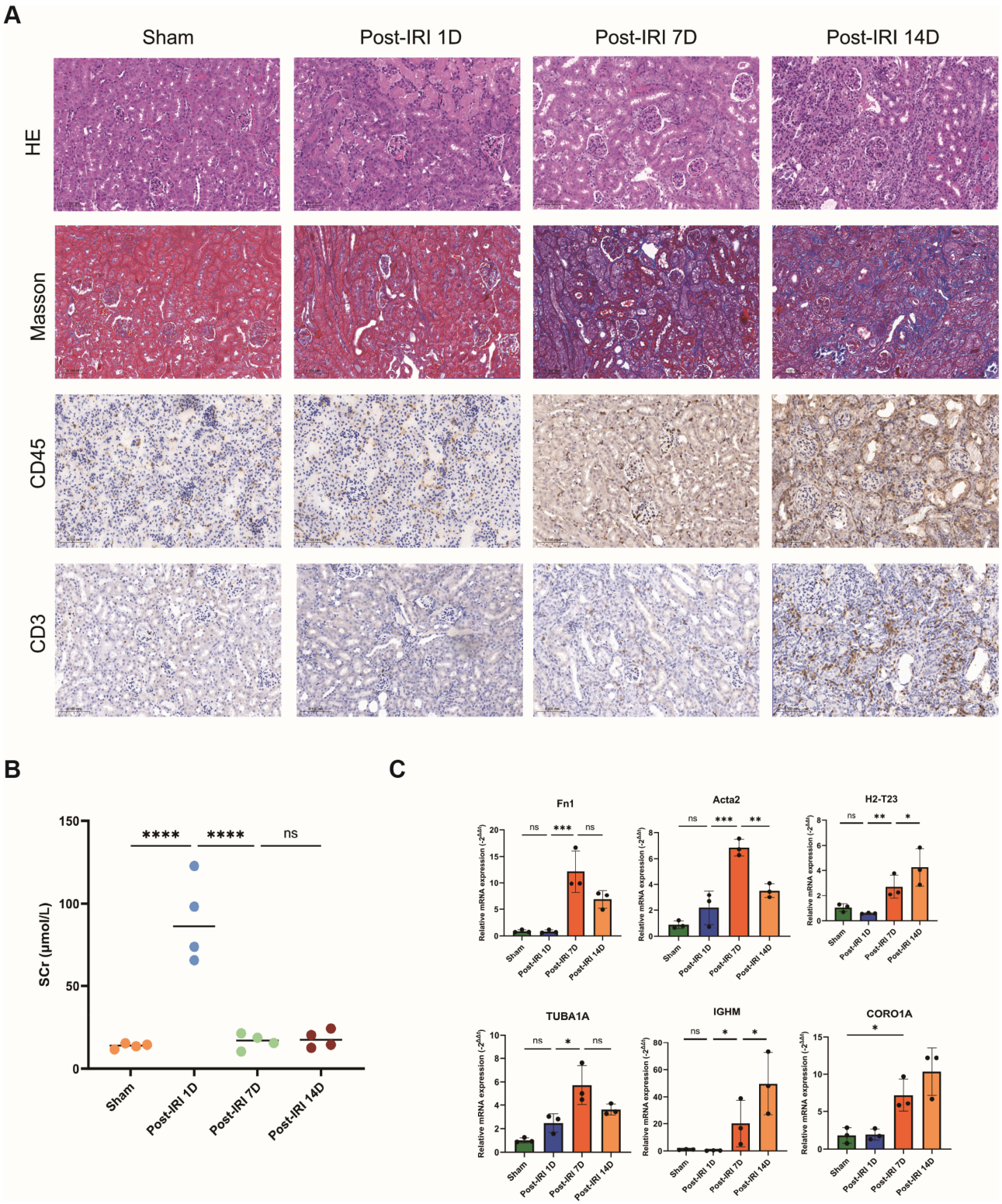

Figure 10 Experimental validation of the hub genes. (**A**) H&E, Masson trichome, and IHC staining in the sham and at 1day, 7days, and 14 days of IRI groups. (**B**) Serum creatinine levels. (**C**) mRNA expression levels of fibrotic gene markers and the four hub genes by qRT-PCR. *, p<0.05; **, p<0.01; ***, p<0.001; ****, p<0.0001; ns, not significant.
Abbreviations: H&E, hematoxylin and eosin; IHC, immunohistochemistry; IRI, ischemia-reperfusion injury; qRT-PCR, real-time quantitative reverse transcription PCR.

increased IL-17A secretion, activation of hepatic stellate cells, and progression of liver fibrosis.[50] Similarly, NK T cells are also metabolically reprogrammed toward a pro-inflammatory phenotype in CKD setting, though their role in IRI remains less defined.[51] These findings establish lactylation influences immune responses and the fibrosis process.

Increased crosstalk between the T cell_2 cluster and monocyte-macrophages, mediated by the MIF-(CD74+CD44) signaling axis, was observed. MIF, a cytokine produced by activated T cells, is a well-established driver of stress-induced pro-inflammatory responses and has been implicated in diverse inflammatory disorders.[52] Notably, a recent study highlighted Cd74-high macrophages as the predominant immune cell population recruited during renal IRI,[53] suggesting a potential pro-inflammatory interplay between lactylation-enriched T cells and monocyte-macrophages. Our findings showed that MIF was generally expressed in the key T cell sub-cluster, especially in the metabolic adaptive T groups upon sub-clustering of the T cell_2 population, further supporting prior evidence that MIF-CD74+CD44 signaling activates T cells and modulates their migration.[54] In the context of renal IRI, CD44 expression has been linked to a significant increase in neutrophil infiltration, and the therapeutic administration of anti-CD44 antibodies has been shown to mitigate renal IRI by reducing neutrophil recruitment.[55] However, MIF-2 in renal tubular epithelial cells has been found to promotes cell regeneration via the secretory leukocyte proteinase inhibitor pathway.[56] These findings suggest the context- and cell type-specific nature of the MIF signaling pathway.[52,57] Further studies are critical to unravel how T cell-specific MIF-CD74/CD44 signaling influences acute injury progression and long-term fibrotic outcomes.

To further investigate the clinical significance of the key T cell_2 cluster, we identified four hub genes (TUBA1A, CORO1A, HLA-E, and IGHM) using hdWGCNA and machine learning models. These genes demonstrated robust diagnostic efficacy for identifying allograft fibrosis and strong prognostic value for graft survival, with the constructed risk scores effectively stratifying graft outcomes. Notably, IGHM, CORO1A, and TUBA1A were associated with decreased GFR and increased SCr levels, underscoring their clinical relevance in renal fibrosis in kidney transplantation patients.

The mechanistic and clinical relevance of these hub genes are supported by prior research demonstrating their involvement in fibrosis. CORO1A, a member of the actin cytoskeleton coronin family, modulates cell cycle progression and apoptosis. Its actin- regulatory activity has been implicated in the functions of T cells and other immune cells.[58,59] Notably, recent findings suggest that CORO1A may also contribute to the pathogenesis of kidney allograft fibrosis by modulating the TGFβ/Smad3 signaling pathway in Th17 CD4+ T cells, one of the predominant pathways of fibrogenesis.[60,61] IGHM expression has shown efficacy in predicting graft loss at 3 years, with higher expression observed in patients with chronic antibody-mediated rejection than in those with operational tolerance,[62] while IGM proteins were observed to be deposit in patients with diabetic nephropathy and were positively associated with fibrosis and inflammation.[63] HLA-E, an emerging immune checkpoint, is associated with donor-specific anti-HLA antibodies, a major determinant of premature and advanced allograft fibrosis, independent of traditional risk factors.[64,65] Finally, TUBA1A, a tubulin superfamily linked to neurodevelopmental disorders,[66] has also been reported as a biomarker in diabetic nephropathy,[67] a major contributor to CKD and kidney fibrosis. Although direct mechanistic associations between lactylation and the four genes remain to be elucidated, several connections are plausible. Lactylation has been implicated in modulating immune responses, autophagy, and cellular proliferation.[68,69] Of particular interest, lactylation has also shown potential in regulating cytoskeleton and microtubules. For example, α-tubulin lactylation by HDAC6 increases microtubule dynamics in neurons and facilitate neurite outgrowth, therefore regulating microtubule functions.[70] This suggests that TUBA1A and CORO1A may be downstream effectors of lactylation-mediated cytoskeletal modulation, while IGHM and HLA-E may reflect lactylation-driven immune regulations. We therefore posit a link in which lactylation-related T cell functional shifts towards cytoskeletal dynamics and immune processes, biasing the milieu toward a pro-inflammatory and pro-fibrotic circuit. Indeed, enrichment analysis showed these genes were associated with apoptosis, phagocytosis, cytoskeletal binding and immunity.

Computational drug sensitivity prediction and molecular docking are promising candidates for preclinical research targeting the identified hub genes. LY294002 and Omipalisib, both selective PI3K/mTOR inhibitors, have demonstrated antifibrotic potential. For instance, LY294002 has been shown to synergize with rapamycin to suppress T cell proliferation more effectively than monotherapy,[71] while Omipalisib has shown clinical potential in treating idiopathic pulmonary fibrosis[72] and exhibits antifibrotic effects in preclinical models of liver fibrosis.[73] In addition to kinase inhibitors, the chemotherapeutic agent floxuridine has emerged as a novel option for keloid management, particularly when combined

with steroids to enhance the therapeutic efficacy.[74] BRAF inhibitors, including the preclinical analog PLX-4720 and its clinically approved derivative vemurafenib, have demonstrated fibrosis-reducing effects in preclinical models of muscular dystrophy and muscle fibrosis.[75] These findings suggest that drug repurposing targeting these four hub genes may offer new avenues for the treatment of fibrosis.

This study has several limitations. First, a recent review[76] summarized the latest identified lactylation-related enzymes; incorporating these genes in future analyses could further refine our findings. Second, although the prognostic model showed acceptable performance, its interpretation requires caution since some gene expression correlations exceeded 0.8, even though VIF values remained within acceptable limits. Third, constructing the model solely on genomic data may oversimplify the biological complexity; integrating clinical parameters could improve both robustness and clinical applicability. Finally, the primarily correlative nature of our findings necessitates experimental validation. To establish causality between lactylation, key genes expression and fibrosis, we are currently assessing lactylation levels of target genes via Western blotting, co-immunoprecipitation, and employing conditional mutation of target genes. Similarly, drug prediction findings are also preliminary, in vitro validation of candidate drugs is also underway.

Conclusions

In conclusion, our study provides novel insights into the potential role of a subset of T cells characterized by elevated lactylation levels and MIF positivity, potentially driven by metabolic reprogramming. By linking lactylation to T-cell activation and pro-inflammatory responses, we highlighted a crucial metabolic shift that may drive fibrosis progression post-transplantation.

Institutional Review Board Statement

The animal study protocol was approved by the Institutional Animal Care Ethics Committee of Beijing Chaoyang Hospital (Ethics No. 24-2016). All human data used in this project adheres to the national legislation guidelines (item 1 and 2 of Article 32 of the Measures for Ethical Review of Life Science and Medical Research Involving Human Subjects). Based on these provisions, the Ethics Committee of Beijing Chaoyang Hospital reviewed this study and deemed it exempt from requiring individual consent (Ethics No. 2025-科-692).

Abbreviations

The following abbreviations are used in this manuscript: DAMP, damage-associated molecular pattern; NETs, neutrophil extracellular traps; PFKFB3, 6-phosphofructo-2-kinase/ fructose-2,6-biphosphatase 3; NF-kB, Nuclear factor kappa-light-chain -enhancer of activated B cells; cGAS, Cyclic GMP-AMP synthase; STING, Stimulator of Interferon Genes; TNF, Tumor necrosis factor; TGFβ, Transforming growth factor beta; MIF, Macrophage migration inhibitory factor; CCL, C-C motif chemokine ligand; FGF, Fibroblast growth factor; TWEAK, TNF superfamily member 12, also known as TNFSF12; LAPTM5, Lysosomal protein transmembrane 5; H2-T23/HLA-E, Major histocompatibility complex, class I, E; RPL, Ribosomal protein; RBM3, RNA binding motif protein 3; SUMO2, Small ubiquitin like modifier 2; RFX3/SRF, Regulatory factor X3/serum response factor; ZNF791, Zinc finger protein 791; LDHA, Lactate dehydrogenase A; SLC5A12, Solute carrier family 5 member 12; SLC16A1, Solute carrier family 16 member 1; CREBH, cAMP-responsive element-binding protein H; IGHM, Immunoglobulin heavy constant Mu; CORO1A/Coro1a, Coronin 1A; TUBA1A/Tuba1a, Tubulin α 1a; FN1, Fibronectin 1; COL1A2, Collagen type I alpha 2 chain; COL1A1, Collagen type I alpha 1 chain; ACTA2, Actin alpha 2; PI3K/mTOR, Phosphatidylinositol 3 -kinase/ mammalian target of rapamycin; BRAF, v-Raf murine sarcoma viral oncogene homolog B.

Data Sharing Statement

Publicly available datasets were used in this study, and are listed in Table 1. The datasets were available from the GEO database (https://www.ncbi.nlm.nih.gov/geo/query/acc.cgi?acc=GSE180420, reference number GSE180420; https://www.ncbi.nlm.nih.gov/geo/query/acc.cgi?acc=GSE22459, reference number GSE22459; https://www.ncbi.nlm.nih.gov/geo/query/acc.cgi?acc=GSE53605, reference number GSE53605; https://www.ncbi.nlm.nih.gov/geo/query/acc.cgi?acc=

GSE76882, reference number GSE76882; https://www.ncbi.nlm.nih.gov/geo/query/acc.cgi?acc=GSE21374, reference number GSE21374). All the data analyzed in this study are available upon request.

Acknowledgments

Xuemeng Qiu, Hao Wang and Yifei Zhang are co-first authors for this work. The authors would like to thank all contributors to the GEO database and the R packages used in this study for their valuable work.

Author Contributions

All authors made a significant contribution to the work reported, whether that is in the conception, study design, execution, acquisition of data, analysis and interpretation, or in all these areas; took part in drafting, revising or critically reviewing the article; gave final approval of the version to be published; have agreed on the journal to which the article has been submitted; and agree to be accountable for all aspects of the work.

Funding

This work was funded by grants from the Beijing Municipal Science and Technology Commission (no. Z221100007422029) and the Clinical Research Incubation Project of Beijing Chao-yang Hospital, Capital Medical University (Project No. CYFH202203).

Disclosure

The authors report no conflicts of interest in this work.

References

1. Zhao H, Alam A, Soo AP, George AJT, Ma D. Ischemia-reperfusion injury reduces long term renal graft survival: mechanism and beyond. *EBioMedicine*. 2018;28:31–42. doi:10.1016/j.ebiom.2018.01.025
2. Lentine KL, Smith JM, Lyden GR, et al. OPTN/SRTR 2023 annual data report: kidney. *Am J Transplant*. 2025;25(2S1):S22–S137. doi:10.1016/j.ajt.2025.01.020
3. Langewisch E, Mannon RB. Chronic allograft injury. *Clin J Am Soc Nephrol*. 2021;16(11):1723–1729. doi:10.2215/CJN.15590920
4. Sanz AB, Sanchez-Nino MD, Ramos AM, Ortiz A. Regulated cell death pathways in kidney disease. *Nat Rev Nephrol*. 2023;19(5):281–299. doi:10.1038/s41581-023-00694-0
5. He L, Wei Q, Liu J, et al. AKI on CKD: heightened injury, suppressed repair, and the underlying mechanisms. *Kidney Int*. 2017;92(5):1071–1083. doi:10.1016/j.kint.2017.06.030
6. Sato Y, Yanagita M. Immune cells and inflammation in AKI to CKD progression. *Am J Physiol Renal Physiol*. 2018;315(6):F1501–F1512. doi:10.1152/ajprenal.00195.2018
7. Kinsey GR, Okusa MD. Role of leukocytes in the pathogenesis of acute kidney injury. *Crit Care*. 2012;16(2):214. doi:10.1186/cc11228
8. Yao W, Chen Y, Li Z, et al. Single cell RNA sequencing identifies a unique inflammatory macrophage subset as a druggable target for alleviating acute kidney injury. *Adv Sci*. 2022;9(12):e2103675. doi:10.1002/advs.202103675
9. Raychaudhuri D, Singh P, Chakraborty B, et al. Histone lactylation drives CD8(+) T cell metabolism and function. *Nat Immunol*. 2024;25(11):2140–2151. doi:10.1038/s41590-024-01985-9
10. Zhang T, Chen L, Kueth G, et al. Lactate's impact on immune cells in sepsis: unraveling the complex interplay. *Front Immunol*. 2024;15:1483400. doi:10.3389/fimmu.2024.1483400
11. Zhang D, Tang Z, Huang H, et al. Metabolic regulation of gene expression by histone lactylation. *Nature*. 2019;574(7779):575–580. doi:10.1038/s41586-019-1678-1
12. Zhu Z, Hu J, Chen Z, et al. Transition of acute kidney injury to chronic kidney disease: role of metabolic reprogramming. *Metabolism*. 2022;131:155194. doi:10.1016/j.metabol.2022.155194
13. Zhang X, Chen J, Lin R, et al. Lactate drives epithelial-mesenchymal transition in diabetic kidney disease via the H3K14la/KLF5 pathway. *Redox Biol*. 2024;75:103246. doi:10.1016/j.redox.2024.103246
14. Fan M, Yang K, Wang X, et al. Lactate promotes endothelial-to-mesenchymal transition via Snail1 lactylation after myocardial infarction. *Sci Adv*. 2023;9(5):eadc9465. doi:10.1126/sciadv.adc9465
15. Xiang T, Wang X, Huang S, et al. Inhibition of PKM2 by shikonin impedes TGF-beta1 expression by repressing histone lactylation to alleviate renal fibrosis. *Phytomedicine*. 2025;136:156324. doi:10.1016/j.phymed.2024.156324
16. Xie N, Tan Z, Banerjee S, et al. Glycolytic reprogramming in myofibroblast differentiation and lung fibrosis. *Am J Respir Crit Care Med*. 2015;192(12):1462–1474. doi:10.1164/rccm.201504-0780OC
17. Wang Y, Li H, Jiang S, et al. The glycolytic enzyme PFKFB3 drives kidney fibrosis through promoting histone lactylation-mediated NF-κB family activation. *Kidney Int*. 2024;106(2):226–240. doi:10.1016/j.kint.2024.04.016
18. Jiang A, Liu J, Wang Y, Zhang C. cGAS-STING signaling pathway promotes hypoxia-induced renal fibrosis by regulating PFKFB3-mediated glycolysis. *Free Radic Biol Med*. 2023;208:516–529. doi:10.1016/j.freeradbiomed.2023.09.011

19. Du S, Zhang X, Jia Y, et al. Hepatocyte HSPA12A inhibits macrophage chemotaxis and activation to attenuate liver ischemia/reperfusion injury via suppressing glycolysis-mediated HMGB1 lactylation and secretion of hepatocytes. *Theranostics*. 2023;13(11):3856–3871. doi:10.7150/thno.82607
20. Zhu L, Zheng Q, Liu X, et al. HMGB1 lactylation drives neutrophil extracellular trap formation in lactate-induced acute kidney injury. *Origin Res Front Immunol*. 2025:15. doi:10.3389/fimmu.2024.1475543
21. Cui H, Xie N, Banerjee S, et al. Lung myofibroblasts promote macrophage profibrotic activity through lactate-induced histone lactylation. *Am J Respir Cell Mol Biol*. 2021;64(1):115–125. doi:10.1165/rcmb.2020-0360OC
22. Balzer MS, Doke T, Yang YW, et al. Single-cell analysis highlights differences in druggable pathways underlying adaptive or fibrotic kidney regeneration. *Nat Commun*. 2022;13(1):4018. doi:10.1038/s41467-022-31772-9
23. Hu C, Li T, Xu Y, et al. CellMarker 2.0: an updated database of manually curated cell markers in human/mouse and web tools based on scRNA-seq data. *Nucleic Acids Res*. 2023;51(D1):D870–D876. doi:10.1093/nar/gkac947
24. Maluf DG, Dumur CI, Suh JL, et al. Evaluation of molecular profiles in calcineurin inhibitor toxicity post-kidney transplant: input to chronic allograft dysfunction. *Am J Transplant*. 2014;14(5):1152–1163. doi:10.1111/ajt.12696
25. Modena BD, Kurian SM, Gaber LW, et al. Gene expression in biopsies of acute rejection and interstitial fibrosis/tubular atrophy reveals highly shared mechanisms that correlate with worse long-term outcomes. *Am J Transplant*. 2016;16(7):1982–1998. doi:10.1111/ajt.13728
26. Park WD, Griffin MD, Cornell LD, Cosio FG, Stegall MD. Fibrosis with inflammation at one year predicts transplant functional decline. *J Am Soc Nephrol*. 2010;21(11):1987–1997. doi:10.1681/ASN.2010010049
27. Einecke G, Reeve J, Sis B, et al. A molecular classifier for predicting future graft loss in late kidney transplant biopsies. *J Clin Invest*. 2010;120 (6):1862–1872. doi:10.1172/JCI41789
28. Moreno-Yruela C, Zhang D, Wei W, et al. Class I histone deacetylases (HDAC1-3) are histone lysine delactylases. *Sci Adv*. 2022;8(3):eabi6696. doi:10.1126/sciadv.abi6696
29. Cheng Z, Huang H, Li M, Liang X, Tan Y, Chen Y. Lactylation-related gene signature effectively predicts prognosis and treatment responsiveness in hepatocellular carcinoma. *Pharmaceuticals*. 2023;16(5):644. doi:10.3390/ph16050644
30. Wu Y, Yang S, Ma J, et al. Spatiotemporal immune landscape of colorectal cancer liver metastasis at single-cell level. *Cancer Discov*. 2022;12 (1):134–153. doi:10.1158/2159-8290.CD-21-0316
31. Morabito S, Reese F, Rahimzadeh N, Miyoshi E, Swarup V. hdWGCNA identifies co-expression networks in high-dimensional transcriptomics data. *Cell Rep Methods*. 2023;3(6):100498. doi:10.1016/j.crmeth.2023.100498
32. Greener JG, Kandathil SM, Moffat L, Jones DT. A guide to machine learning for biologists. *Nat Rev Mol Cell Biol*. 2022;23(1):40–55. doi:10.1038/s41580-021-00407-0
33. Nguyen QH, Ly H-B, Ho LS, et al. Influence of data splitting on performance of machine learning models in prediction of shear strength of soil. *Mathematic Probl Engine*. 2021;2021(1):4832864. doi:10.1155/2021/4832864
34. Tian D, Yan HJ, Huang H, et al. Machine learning-based prognostic model for patients after lung transplantation. *JAMA Network Open*. 2023;6(5): e2312022. doi:10.1001/jamanetworkopen.2023.12022
35. Liu H, Zhang W, Zhang Y, et al. Mime: a flexible machine-learning framework to construct and visualize models for clinical characteristics prediction and feature selection. *Comput Struct Biotechnol J*. 2024;23:2798–2810. doi:10.1016/j.csbj.2024.06.035
36. Zeng D, Fang Y, Qiu W, et al. Enhancing immuno-oncology investigations through multidimensional decoding of tumor microenvironment with IOBR 2.0. *Cell Rep Methods*. 2024;4(12):100910. doi:10.1016/j.crmeth.2024.100910
37. Aibar S, Gonzalez-Blas CB, Moerman T, et al. SCENIC: single-cell regulatory network inference and clustering. *Nat Methods*. 2017;14 (11):1083–1086. doi:10.1038/nmeth.4463
38. Reinhold WC, Sunshine M, Liu H, et al. CellMiner: a web-based suite of genomic and pharmacologic tools to explore transcript and drug patterns in the NCI-60 cell line set. *Cancer Res*. 2012;72(14):3499–3511. doi:10.1158/0008-5472.CAN-12-1370
39. An S, Yao Y, Hu H, et al. PDHA1 hyperacetylation-mediated lactate overproduction promotes sepsis-induced acute kidney injury via Fis1 lactylation. *Cell Death Dis*. 2023;14(7):457. doi:10.1038/s41419-023-05952-4
40. She H, Hu Y, Zhao G, et al. Dexmedetomidine ameliorates myocardial ischemia-reperfusion injury by inhibiting MDH2 lactylation via regulating metabolic reprogramming. *Adv Sci*. 2024;11(48):e2409499. doi:10.1002/advs.202409499
41. Yu W, Kong Q, Jiang S, et al. HSPA12A maintains aerobic glycolytic homeostasis and Histone3 lactylation in cardiomyocytes to attenuate myocardial ischemia/reperfusion injury. *JCI Insight*. 2024;9(7). doi:10.1172/jci.insight.169125
42. Sun Z, Gao Z, Xiang M, et al. Comprehensive analysis of lactate-related gene profiles and immune characteristics in lupus nephritis. *Front Immunol*. 2024;15:1329009. doi:10.3389/fimmu.2024.1329009
43. Wang N, Wang W, Wang X, et al. Histone lactylation boosts reparative gene activation post-myocardial infarction. *Circ Res*. 2022;131 (11):893–908. doi:10.1161/CIRCRESAHA.122.320488
44. Li Y, Min X, Zhang X, et al. HSPA12A promotes c-Myc lactylation-mediated proliferation of tubular epithelial cells to facilitate renal functional recovery from kidney ischemia/reperfusion injury. *Cell Mol Life Sci*. 2024;81(1):404. doi:10.1007/s00018-024-05427-5
45. Wu H, Huang H, Zhao Y. Interplay between metabolic reprogramming and post-translational modifications: from glycolysis to lactylation. *Front Immunol*. 2023;14:1211221. doi:10.3389/fimmu.2023.1211221
46. Wu X, Liu C, Zhang C, et al. The role of lactate and lactylation in the dysregulation of immune responses in psoriasis. *Clin Rev Allergy Immunol*. 2025;68(1):28. doi:10.1007/s12016-025-09037-2
47. Peng M, Yin N, Chhangawala S, Xu K, Leslie CS, Li MO. Aerobic glycolysis promotes T helper 1 cell differentiation through an epigenetic mechanism. *Science*. 2016;354(6311):481–484. doi:10.1126/science.aaf6284
48. Haas R, Smith J, Rocher-Ros V, et al. Lactate regulates metabolic and pro-inflammatory circuits in control of T cell migration and effector functions. *PLoS Biol*. 2015;13(7):e1002202. doi:10.1371/journal.pbio.1002202
49. Papadopoulou G, Xanthou G. Metabolic rewiring: a new master of Th17 cell plasticity and heterogeneity. *FEBS J*. 2022;289(9):2448–2466. doi:10.1111/febs.15853
50. Chen W, Wang P, Xie Y, et al. Histone lactylation-augmented IRF4 is implicated in arsenite-induced liver fibrosis via modulating Th17 cell differentiation. *Chem Biol Interact*. 2025;414:111507. doi:10.1016/j.cbi.2025.111507
51. Li J, Yang Y, Wang Y, Li Q, He F. Metabolic signatures of immune cells in chronic kidney disease. *Expert Rev Mol Med*. 2022;24:e40. doi:10.1017/erm.2022.35

52. Jankauskas SS, Wong DWL, Bucala R, Djudjaj S, Boor P. Evolving complexity of MIF signaling. *Cell Signal*. 2019;57:76–88. doi:10.1016/j.cellsig.2019.01.006
53. Zhang YL, Tang TT, Wang B, et al. Identification of a novel ECM remodeling macrophage subset in AKI to CKD transition by integrative spatial and single-cell analysis. *Adv Sci*. 2024;11(38):e2309752. doi:10.1002/advs.202309752
54. Zhang L, Woltering I, Holzner M, et al. CD74 is a functional MIF receptor on activated CD4(+) T cells. *Cell Mol Life Sci*. 2024;81(1):296. doi:10.1007/s00018-024-05338-5
55. Kim MS, Lee KH, Lee WM, Jun JH, Kim DH. CD44 disruption attenuates murine hepatic ischemia/reperfusion injury. *J Korean Med Sci*. 2011;26(7):919–926. doi:10.3346/jkms.2011.26.7.919
56. Ochi A, Chen D, Schulte W, et al. MIF-2/D-DT enhances proximal tubular cell regeneration through SLPI- and ATF4-dependent mechanisms. *Am J Physiol Renal Physiol*. 2017;313(3):F767–F780. doi:10.1152/ajprenal.00683.2016
57. Tilstam PV, Schulte W, Holowka T, et al. MIF but not MIF-2 recruits inflammatory macrophages in an experimental polymicrobial sepsis model. *J Clin Invest*. 2021;131(23). doi:10.1172/JCI127171
58. Foger N, Rangell L, Danilenko DM, Chan AC. Requirement for coronin 1 in T lymphocyte trafficking and cellular homeostasis. *Science*. 2006;313(5788):839–842. doi:10.1126/science.1130563
59. Shaverskyi A, Hegermann J, Brand K, Lee KH, Foger N. Coronin 1a-mediated F-actin disassembly controls effector function in murine neutrophils. *Redox Biol*. 2025;82:103618. doi:10.1016/j.redox.2025.103618
60. Niu X, Xu C, Cheuk YC, et al. Characterizing hub biomarkers for post-transplant renal fibrosis and unveiling their immunological functions through RNA sequencing and advanced machine learning techniques. *J Transl Med*. 2024;22(1):186. doi:10.1186/s12967-024-04971-9
61. Kaminski S, Hermann-Kleiter N, Meisel M, et al. Coronin 1A is an essential regulator of the TGFbeta receptor/SMAD3 signaling pathway in Th17 CD4(+) T cells. *J Autoimmun*. 2011;37(3):198–208. doi:10.1016/j.jaut.2011.05.018
62. Hruba P, Klema J, Le AV, et al. Novel transcriptomic signatures associated with premature kidney allograft failure. *EBioMedicine*. 2023;96:104782. doi:10.1016/j.ebiom.2023.104782
63. Tserga A, Saulnier-Blache JS, Palamaris K, et al. Complement cascade proteins correlate with fibrosis and inflammation in early-stage type 1 diabetic kidney disease in the Ins2Akita mouse model. *Int J Mol Sci*. 2024;25(3). doi:10.3390/ijms25031387
64. Liu X, Song J, Zhang H, et al. Immune checkpoint HLA-E:CD94-NKG2A mediates evasion of circulating tumor cells from NK cell surveillance. *Cancer Cell*. 2023;41(2):272–287e9. doi:10.1016/j.ccell.2023.01.001
65. Gosset C, Viglietti D, Rabant M, et al. Circulating donor-specific anti-HLA antibodies are a major factor in premature and accelerated allograft fibrosis. *Kidney Int*. 2017;92(3):729–742. doi:10.1016/j.kint.2017.03.033
66. Maillard C, Roux CJ, Charbit-Henrion F, et al. Tubulin mutations in human neurodevelopmental disorders. *Semin Cell Dev Biol*. 2023;137:87–95. doi:10.1016/j.semcdb.2022.07.009
67. Wu S, Li W, Chen B, et al. Gene-based network analysis reveals prognostic biomarkers implicated in diabetic tubulointerstitial injury. *Dis Markers*. 2022;2022:2700392. doi:10.1155/2022/2700392
68. Ren H, Tang Y, Zhang D. The emerging role of protein L-lactylation in metabolic regulation and cell signalling. *Nat Metab*. 2025;7(4):647–664. doi:10.1038/s42255-025-01259-0
69. Ye L, Jiang Y, Zhang M. Crosstalk between glucose metabolism, lactate production and immune response modulation. *Cytokine Growth Factor Rev*. 2022;68:81–92. doi:10.1016/j.cytogfr.2022.11.001
70. Sun S, Xu Z, He L, et al. Metabolic regulation of cytoskeleton functions by HDAC6-catalyzed alpha-tubulin lactylation. *Nat Commun*. 2024;15(1):8377. doi:10.1038/s41467-024-52729-0
71. Breslin EM, White PC, Shore AM, Clement M, Brennan P. LY294002 and rapamycin co-operate to inhibit T-cell proliferation. *Br J Pharmacol*. 2005;144(6):791–800. doi:10.1038/sj.bjp.0706061
72. Lukey PT, Harrison SA, Yang S, et al. A randomised, placebo-controlled study of omipalisib (PI3K/mTOR) in idiopathic pulmonary fibrosis. *Eur Respir J*. 2019;53(3):1801992. doi:10.1183/13993003.01992-2018
73. Gore E, Bigaeva E, Oldenburger A, et al. PI3K inhibition reduces murine and human liver fibrogenesis in precision-cut liver slices. *Biochem Pharmacol*. 2019;169:113633. doi:10.1016/j.bcp.2019.113633
74. Ekstein SF, Wyles SP, Moran SL, Meves A. Keloids: a review of therapeutic management. *Int J Dermatol*. 2021;60(6):661–671. doi:10.1111/ijd.15159
75. Oliveira-Santos A, Dagda M, Wittmann J, Smalley R, Burkin DJ. Vemurafenib improves muscle histopathology in a mouse model of LAMA2-related congenital muscular dystrophy. *Dis Model Mech*. 2023;16(6). doi:10.1242/dmm.049916
76. Zong Z, Ren J, Yang B, Zhang L, Zhou F. Emerging roles of lysine lactyltransferases and lactylation. *Nat Cell Biol*. 2025;27(4):563–574. doi:10.1038/s41556-025-01635-8